Ph. D. DISSERTATION

THIN FILM TRANSISTORS USING METAL OXIDES AND 2D NANOMATERIALS: PERFORMANCE OPTIMIZATION AND APPLICATION TO QUANTUM DOT LIGHT-EMITTING DIODES

금속 산화물 및 이차원 나노 물질 기반의 박막 트랜지스터: 성능 최적화 및 양자점 발광 다이오드에 대한 응용

BY

GEUN WOO BAEK

AUGUST 2021

DEPARTMENT OF
ELECTRICAL AND COMPUTUER ENGINEERING
COLLEGE OF ENGINEERING
SEOUL NATIONAL UNIVERSITY

THIN FILM TRANSISTORS USING METAL OXIDES AND 2D NANOMATERIALS: PERFORMANCE OPTIMIZATION AND APPLICATION TO QUANTUM DOT LIGHT-EMITTING DIODES

금속 산화물 및 이차원 나노 물질 기반의 박막 트랜지스터: 성능 최적화 및 양자점 발광 다이오드에 대한 응용

지도교수 곽 정 훈

이 논문을 공학박사 학위논문으로 제출함

2021 년 8 월 서울대학교 대학원

전기정보 공학부

백 근 우

백근우의 공학박사 학위논문을 인준함

2021 년 8 월

위 원 장 : _____

부위원장 : _____

위 원 : _____

위 원 : _____

위 원 : _____

Abstract

THIN FILM TRANSISTORS USING METAL OXIDES AND 2D NANOMATERIALS: PERFORMANCE OPTIMIZATION AND APPLICATION TO QUANTUM DOT LIGHT-EMITTING DIODES

GEUN WOO BAEK
DEPARTMENT OF ELECTRICAL AND COMPUTER ENGINEERING
COLLEGE OF ENGINEERING
SEOUL NATIONAL UNIVERSITY

The development of electronic displays integrated with Thin Film Transistors (TFTs) has been great interests due to their superb merits. For the past decades, several studies have been reported for the flat-panel displays (FPDs) such as active-matrix liquid crystal display (LCD) and organic light-emitting diode (OLED). Despite of these excellent achievements, progress of p-type oxide/nano semiconductors and

operation of quantum dot light-emitting diode (QLED) driven by backplane TFTs are limited. This is because the electrical characteristics of p-type semiconductor have low mobility, high off current, and device instability. In this sense, we investigated p-type oxide/nano material-based TFTs and colloidal quantum dot light-emitting diodes (QLEDs) for the afore-mentioned application.

First, we implemented p-type tin oxide (SnO) TFTs with spray-coated single-wall carbon nanotube (SWNTs) as source and drain electrodes for their electrical characteristics as alternative electrodes formed of nanowire structures, which are potentially attractive for flexible electronics. The device architecture of SnO TFTs with a polymer etch stop layer (SU-8) enables the selective etching of SWNTs in a desired region without the detrimental effects of SnO channel layers. In addition, SnO TFTs with SWNT electrodes as substitutes successfully demonstrate decent width normalized electrical contact properties (~1 kΩ cm), field effect mobility (~0.69 cm^2/Vs), sub-threshold slope (~0.4 V/dec), and current on-off ratio (I_{on}/I_{off} ~ 3.5×10^3). Furthermore, temperature-dependent electrical contact and channel properties elucidate SnO channel transports with an activation energy of 3×10^{-3} eV, interpreted as a negligible level of valence-band tail states, together with decent contact resistance comparable to that of Ni electrodes.

Second, we firstly demonstrated the QLEDs operation modulated by p (or n-type) $MoTe_2$ TFTs with the realization of complementary type transistor. In this study, molecular doping by Poly-L-lysine (PLL) as an electron dopant is adopted for a type conversion of $MoTe_2$ TFTs, and surface ligand modification is utilized for the improvement of QLED performance. In this regard, the PLL treatment achieves the outstanding type conversion of $MoTe_2$ TFTs without any degradation of electrical properties, leading to securing reliable p (or n-type) devices, thus, availability of complementary circuits. Furthermore, ligand modified QDs capped with octylamine

result in balanced electron/hole injection in QLEDs, yielding improved current efficiency (η_A =13.9 cd/A) and longer lifetimes (T_{50} = 66 h at L0 = 3000 cd/m^2). As a result, $MoTe_2$ TFTs demonstrate their capabilities to drive the QLEDs for the envisioned application including display backplane transistor with decent switching properties, immunity for generation of photocurrent, and operation stability.

In this thesis, we discuss the oxide/nano material based TFTs and ligand modified bottom emitting red QLEDs for many promising applications. Our research achievements using p-type SnO and $MoTe_2$ as backplane TFTs, and CdSe QLED as novel display device can be used in potentially envision fields for the convergence research.

Keywords: Quantum Dot Based Light-Emitting Diodes, SnO TFTs, $MoTe_2$ TFTs, Ligand modification, type controllability, Single-walled carbon nanotubes.

Student Number: 2017-37091

Contents

List of Figures

List of Tables

Chapter 1

Introduction

1.1 An Overview of Thin Film Transistors

After first fabrication in 1962 [1], thin film transistors (TFTs), which are type of field-effect transistor (FETs), are fundamentally regarded as one of electronic components from mobile phone to flat panel Displays (FPDs). Compared to a metal oxide semiconductor field effect transistor (MOSFET) exploiting only a silicon wafer as semiconductor and substrate, a TFT, which is available at different substrate using glass, has superb advantages such as a low-cost, an easy and reliable processibility on large area devices. Currently, semiconducting material as active layer of TFTs is being used for organic light-emitting didoes (OLEDs) and liquid crystal displays (LCDs).

To realize the high performance of display devices, fast response time, panel flexibility, high resolution, and reliability are dispensable for FPDs. For example, the

required carrier mobility (μ) of backplane TFTs to achieve high resolution and high speed of OLED displays should exceed 10 [cm^2/vs]. In this regard, Fig 1.1 shows the representative candidates of active materials to fulfill this requirement. Also, as the progress of advanced display devices has been accelerated, flexible semiconducting material attracts a lot of attentions due to their mechanical flexibility.

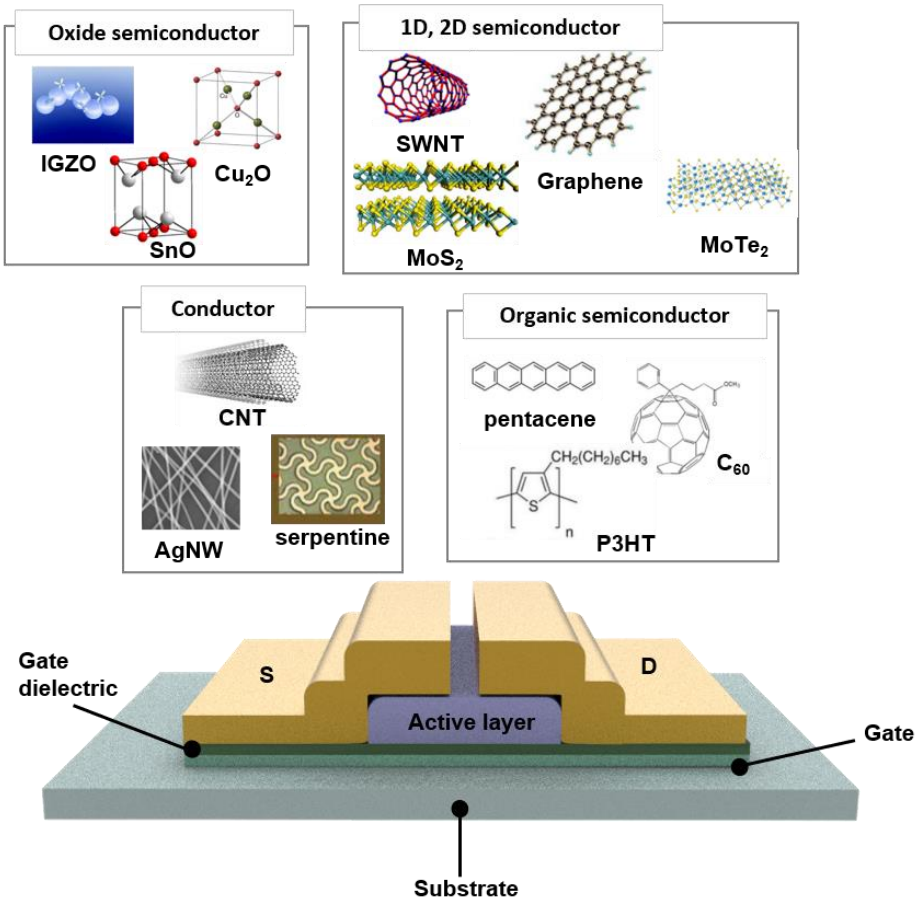

Figure 1.1 Device structure of thin film transistors and their representative materials as active layer and conductor.

As shown in Fig 1.2, mobility versus mechanical flexibility was investigated using amorphous/polycrystalline silicon, organic semiconductor, single-walled carbon nanotubes (SWNTs), amorphous metal oxide semiconductor, and transition metal dichalcogenides (TMDCs) for FPDs. In this thesis, we focus on the metal oxide semiconductor and TMDCs as active layer and SWNTs as conductor for the next generation displays.

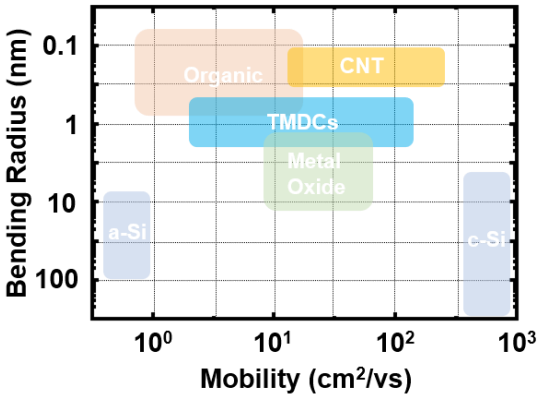

Figure 1.2 Charge carrier mobility vs flexibility of various semiconductor materials for thin film transistors (Holst center) [2].

1.1.1 Oxide Semiconductor

After demonstration of the indium gallium zinc oxide (IGZO) TFTs by Nomura *et al.* in 2004, an intensive progress in amorphous oxide semiconductor (AOS) TFTs has been studied for the next FPDs applications in Fig. 1.3 [3]. Compared to a-Si for LCD display, AOS TFTs have much higher electrical properties with high field effect mobility (> 10 cm^2/vs). Also, AOS TFTs have been regarded as the promising candidate instead of low temperature poly si (LTPS) which has non-uniformity in large area devices due to grain boundary of poly-Si [4]. In addition to benefits with excellent electrical properties, AOS TFTs are compatible with conventional process scheme using sputtering deposition at room temperature (RT) [5]. However, most of studies in oxide semiconductor have been researched in n-type AOS TFTs, especially in a-IGZO and ZnO.

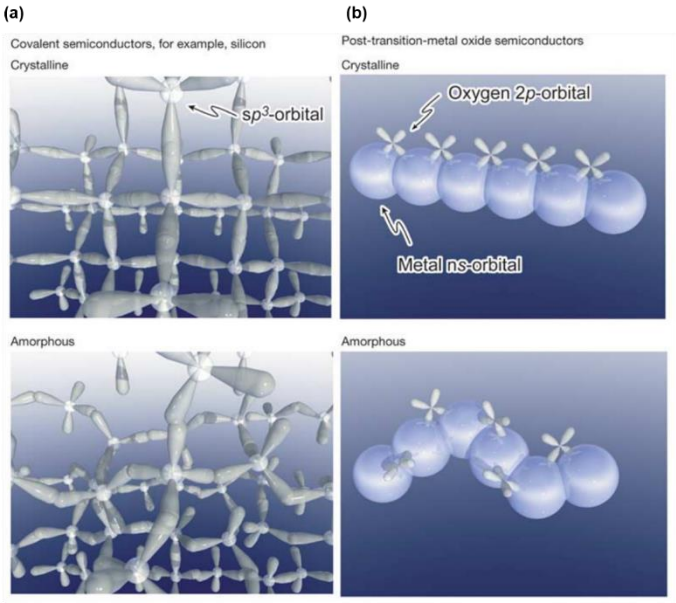

Figure 1.3 Schematic orbital structure for the conduction band minimum (CBM) in (a) covalent semiconductor and (b) amorphous oxide semiconductor [3].

In this regard, p-type oxide semiconductor has attractive attention for achieving the complementary logic circuit with oxide semiconductor TFTs. Especially, there are a very limited number of p-type oxide semiconductor such as Cu_2O, NiO, and SnO. Among these candidates, SnO shows excellent p-type conductivity due to the formation of a substantial amount of native acceptor in Fig. 1.4. In **chapter 3**, we focused on p-type SnO TFTs with spray-coated SWNTs for the potential application such as wearable devices.

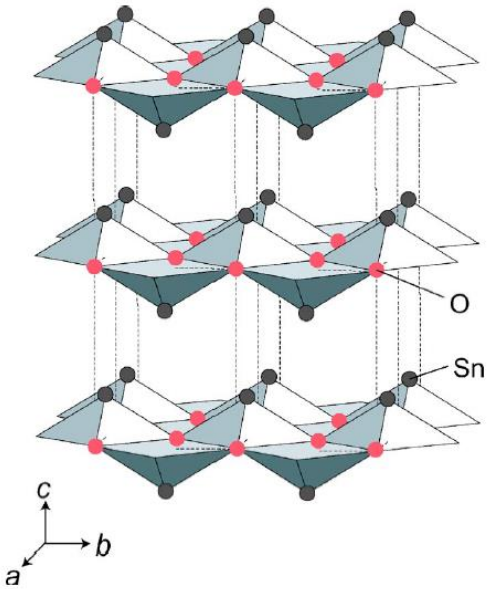

Figure 1.4 A pyramid structure of SnO [6].

1.1.2 Transition Dichalcogenides (TMDCs)

Recently, TMDCs , which are composed of transition metal (e.g., Mo, W, Ta, Ti, Hf, Zr, Cr, V, and Nb) and chalcogen (e.g., S, Se, and Te), have gained tremendous interests in electronic/optoelectronic applications owing to prominent optical/elelctrical properties, a controllable bandgap, superior electrostatic gate coupling, and immunity to a short channel effect [7-11] in Fig. 1.5. In particular, TMDCs have been researched as the important electronic devices such as logic gate circuits, complementary metal-oxide-semiconductor (CMOS) inverters, and active matrix backplanes due to its decent carrier mobility and the absence of surface dangling bonds [7]. For the application of optoelectronic devices, TMDs have one of the excellent candidates to realize the switching device for organic (or quantum dot) light-emitting diode (OLED/QLED) displays in lieu of conventioanl Si technology. Basis of this exceptional properties, there are few atemps to adpot TMDC material as the switching layer. For example, Choi et al. reported the ultrathin flexible OLED display driven by MoS_2 based TFTs [12]. Based on the MoS_2 TFTs arrays, flexible active matrixed-OLED display was well operated even in a highly deformed state. However, most of studies are limited to the single type of transistor such as exploiting MoS_2 (n-type) and WSe_2 (p-type) materials owing to the Fermi-level pinning.

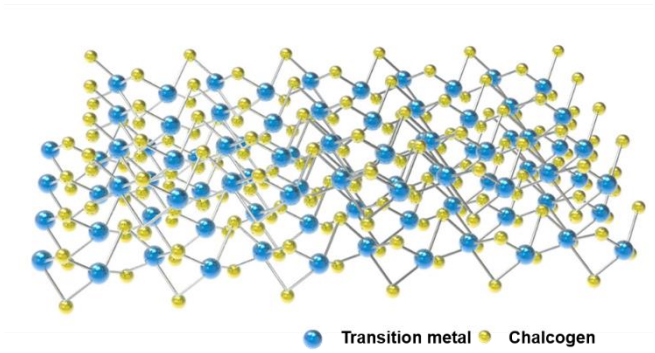

Figure 1.5 Crystal structure of transition metal dichalcogenide (TMDC).

In this regard, there are several ways to convert the type of TMD such as partial modification of Mo (or W) using Nb atom, mild plasma treatment (He or H_2) on WSe_2 and chemical doping by molecular reductants and oxidants on MoS_2 (or WSe_2) [13]. Despite these preiviously reported works, practical methodologies have been limited due to low gate controllability, instability of chemcial doping, and difficulty of process scheme [14]. So, we adopted a molybdenum ditelluride ($MoTe_2$) exhibiting a negligible Fermi-level pinning phenomenon and the availability of type conversion. Indeed, p-type characteristics of $MoTe_2$ are attributed to the adsorption of oxygen molecules on the channel layer. Therefore, the polarity of p-type $MoTe_2$ with 0.9 eV (indirect bandgap) and 1.1 eV (direct bandgap) can be controlled by a various doping process. As we know, previous studies in literature have been focused on such as (i) the insertion of high-k oxide dopant layer to reduce the Schottky barrier height (ii) inducing rapid thermal annealing (RTA) for benzyl viologen (BV) doping, and (iii) deep-ultraviolet (DUV) irradiation in N_2 and O_2 gas ambient [15-17]. In this sense, we demonstrated not only the type converted $MoTe_2$ TFTs via PLL treatment but also the operation of QLED display with light-insensitive $MoTe_2$ TFTs in **Chapter 4**.

1.2 An Overview of Quantum Dot Light-Emitting Diodes

Recently, colloidal quantum dots (QDs) have received a lot of attentions due to their superb properties such as size-tunable bandgap engineering, high photoluminescence quantum yield (PLQY), and narrow full-width at half-maximum (FWHM). These excellent properties make QDs practically adoptable in LEDs, solar cells, photo detector, biomedicine, and wearable devices [18-26]. Since the first demonstration of QD based electroluminescence devices by the Colvin *et al.*, intensive efforts have been conducted to achieve high performance EL device with high external quantum efficiency (EQE) and high brightness [27, 28]

As with already commercialized OLEDs, QDs as a promising material exhibit excellent features. As shown in Fig. 1.6(a), a photographical image denotes the size-dependent bandgap tunability of QDs and confinement of electron and hole wave functions. Superior to OLEDs, FWHM of QLEDs has narrow bandwidth less than 30 nm. Figure 1.6(b) shows the difference of FWHM between Cd-based QLEDs and typical OLEDs, which are wider bandwidth due to the vibronic states in organic dyes. Furthermore, the narrow bandwidth and high color purity of QDs can make them wide color gamut in CIE 1931 color space in Fig. 1.6(c). Based on these excellent properties, remarkable progress of QDs is being conducted like QD-OLED display in Fig. 1.7.

Since the first fabrication of QLEDs in 1994 by Colin *et al.*, device performance of Cd-based QLEDs has been gradually increased. In the early 1990s, the device structure of QLEDs is very similar with polymer light-emitting diodes (PLEDs). Also, QDs without formation of shell for the elimination of defect sites were low efficiency and short longevity. To enhance the device performance and durability, P. Alivisatos's group reported core/shell structured QDs, which led to photostability and electronic accessibility for the use in optoelectronic devices [29].

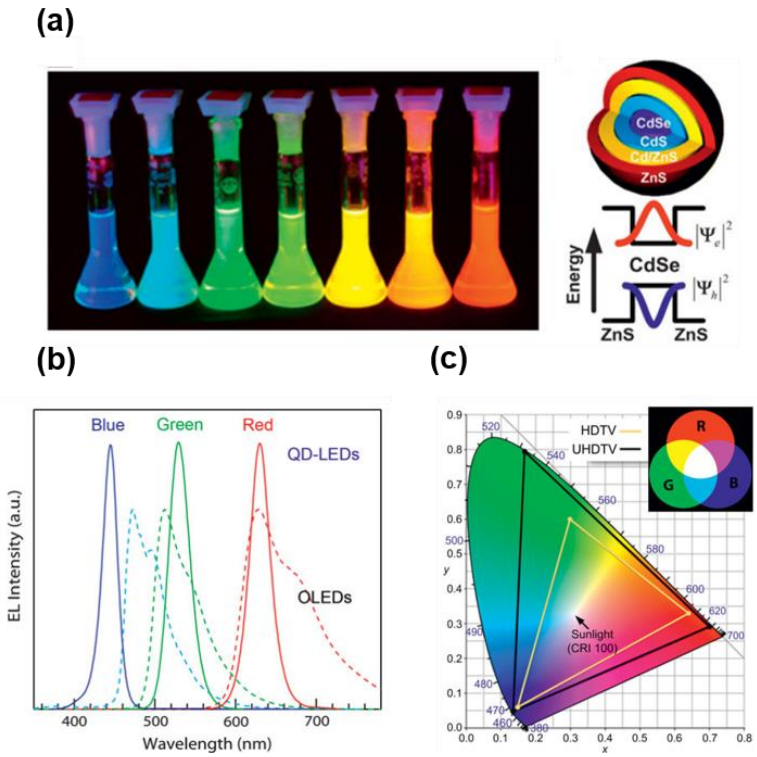

Figure 1.6 (a) A size controllable color change of CdSe/ZnS core shell QDs and their schematic structure and radial probability functions for which electron (red curve) and hole (blue curve) are displayed. (b) comparison of R, G, B QLEDs (solid lines) and those of OLEDs (dashed lines). (c) International commission on illumination (CIE) chromaticity diagram for qualifying the quality of display, TVs, and other devices. [30, 31]

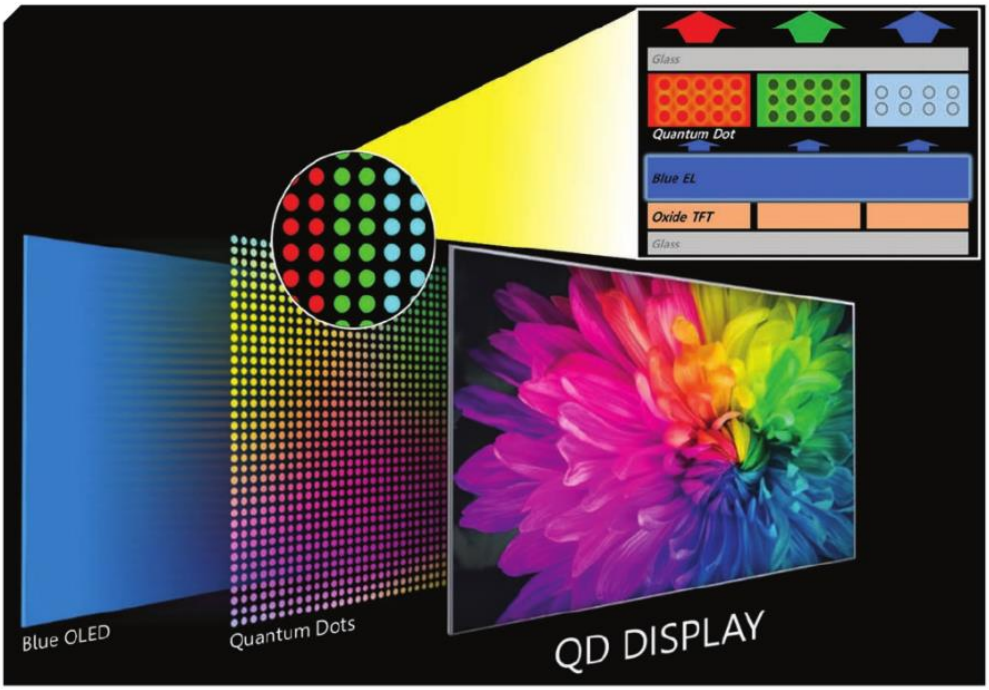

Figure 1.7 A schematic illustration of QD display. [SID 2021]

Although the device performance was remarkably enhanced compared to PLEDs, the instability of organic transport layer and inefficient carrier injection was critical issues. To solve this problem, there were many attempts including phase-segregation method, cross-linkable polymer hole transport layer (HTL), and inorganic HTL. However, these approaches brought unintended demerits such as high cost and complicated fabrication scheme unlike the advantage of conventional QLEDs. In this regard, Kwak *et al.* reported inverted device structure to achieve the bright and efficient QLEDs in 2012 [32]. Based on the inverted structure, device performance of red, green, and blue emitting CdSe QLEDs was remarkably increased owing to adoption of inorganic metal oxide semiconductor using ZnO nanoparticles and a robust fabrication step for continuous QD deposition.

From this point, tremendous improvement of device performance in QLEDs has been actively reported in Fig. 1.8. In 2014, X. Dai *et al.* reported a highly efficient Cd-based red QLED with a low turn-on at 1.7 V and high EQE up to 20.5% [33]. The highly efficient QLEDs was achieved by inserting an insulating layer between emissive layer and oxide electron transport layer. This methodology makes this device comparable to state-of-the-art vacuum deposited QLEDs at that time. Besides, H. Moon *et al.* efficiently controlled the negative dipole moment using ligand modification and thus achieved a high maximum EQE (24.8%) [36]. Interestingly, J. Song *et al.* reported hybrid type QLEDs, exhibiting extremely high peak EQE (> 30%) and very low efficiency roll-off at high current density (150 mA cm^{-2}) [37]. These extraordinary properties are coming from not only use of a gradient core/shell composition with thicker ZnSe interlayer shell and ultrathin ZnS outer shell but also 2-ethylhexane-1-thiol (EHT) surface ligand modification. Thanks to these efforts, QLEDs are expected to be used in future applications such as mobile phone, TVs, and wearable devices.

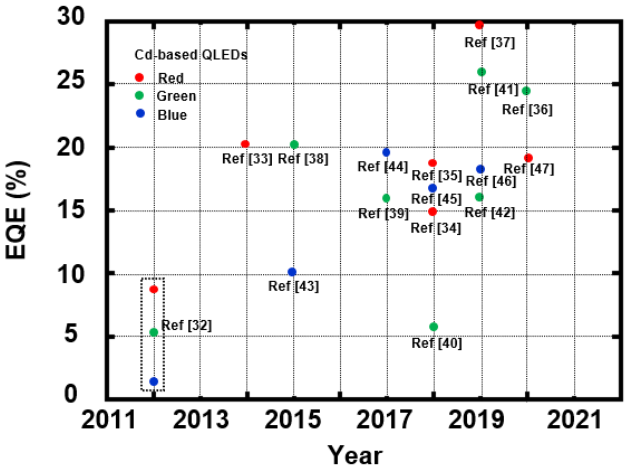

Figure 1.8 The maximum EQE of red, green, and blue QLEDs as a function of year [32-47].

1.3 Outline of Thesis

This thesis consists of five chapters, including the Introduction and Conclusion. In the introduction of **Chapter 1**, an overview of thin film transistor and quantum dot light-emitting diodes and their previous research papers are briefly explained. **Chapter 2** includes material preparation: the methods used to prepare ZnO nanoparticles and type I red $CdSe/Cd_{1-x}Zn_xS$ QDs used in this thesis. In addition, the characterization methods for TFTs and QLEDs devices are summarized in this chapter, and the electrical and morphological characterization methods for thin films used in this thesis are depicted. Characterization methods for electrical and morphological characteristics of thin films are also described in this Chapter. In **Chapter 3**, we fabricated p-type SnO TFTs with spray-coated SWNTs as alternative electrodes of a source and a drain. Moreover, by analyzing current–voltage characteristics of the SnO TFTs depending on substrate temperature, we systematically measured the intrinsic field effect mobility as well as electrical contact properties for SnO TFTs to understand (or validate) feasible electrical properties of spray-coated SWNTs with SnO films, compared to previously reported metal electrodes. In **Chapter 4**, we firstly demonstrated the operation of ligand exchanged QLEDs display driven by $MoTe_2$ TFTs with achievement of the systematic and reliable type conversion. To provide sufficient currents to QLEDs without electrical degradation even under illumination from UV to near-IR range, light-insensitive $MoTe_2$ TFTs were adopted. Furthermore, type controllability of $MoTe_2$ TFTs via PLL treatment as an electron dopant can be one of options to minimize the pixel variation due to mismatched display configuration using n-type TFTs and normal structure of LEDs. In addition to backplane TFTs, octylamine ligands were utilized to control the VBM of QDs, minimize the insulating properties of oleic acid capped-QDs, and thus efficiently

optimize electron-hole charge balance. As with ligand modification methodology, the improved current efficiency (η_A =13.9 cd/A) and longer lifetimes (T_{50} = 66 h at L_0 = 3000 cd/m^2) were observed.

Finally, in **Chapter 5**, we summarize our work and make concluding remarks.

Chapter 2

Experimental Methods

2.1 Materials

2.1.1 Synthesis of ZnO Nanoparticles

ZnO nanoparticles. First, 2 g of zinc acetate dehydrate ($Zn(CH_3COO)_2 \cdot 2H_2O$) and 80 mL of methanol were mixed in a three neck flask. When the temperature grew up to 60 ℃ in N_2 atmosphere, potassium hydroxide (KOH) dissolved in methanol (23.25 mg mL^{-1}) was added into the flask at the rate of 238.5 mL h^{-1}. After 150 min of reaction, the ZnO NPs were sunk down for 12 h. After that, the solution was centrifuged at 4000 rpm for 3 min to extract pure ZnO NPs from the mixture solution. The ZnO NPs were redispersed in 1-butanol.

2.1.2 Synthesis of Red-Light-Emitting CdSe/$Cd_{1-x}Zn_xS$ Quantum Dots

Materials for QD synthesis: Zinc acetate ($Zn(ac)_2$, 99.99%), sulfur (S, 99.998%), selenium (Se, 99.99%), oleic acid (OA, 99%), and 1-octadecene (ODE, 99%) were purchased from UniAm (Korea). n-Trioctylphosphine (TOP, technical grade, 90%) and octylamine (OcA, 99%) were purchased from Sigma Aldrich. Cadmium oxide (CdO, 99.95%), myristic acid (MA, >99%) and 1-dodecanethiol (DDT, >98%) were

purchased from Alfa Aesar. All chemicals are used as received without further purification.

Precursors for QD synthesis: a 0.5 M cadmium oleate ($Cd(OA)_2$) stock solution, a 0.5 M zinc oleate ($Zn(OA)_2$) stock solution, a 2 M TOPSe solution, and a 2 M TOPS solution were prepared as cation and anion precursors, respectively. To prepare the $Cd(OA)_2$ stock solution, CdO (30 mmol), OA (30 mL), and ODE (30 mL) were loaded in a reaction flask and degassed at 110 °C for 1 h. The flask was backfilled with Ar, heated to 300 °C to obtain a clear $Cd(OA)_2$ solution, cooled to 110 °C, and degassed for 1 h. To prepare the $Zn(OA)_2$ stock solution, $Zn(ac)_2$ (100 mmol) and OA (100 mL) were placed in a flask and degassed for 1 h. After degassing, the reaction temperature was raised to 160 °C and maintained until the formation of the $Zn(OA)_2$ solution was complete. The flask was filled with Ar, and the solution was diluted with degassed ODE to a concentration of 0.5 M. To prepare 2 M TOPS and 2 M TOPSe stock solutions, S or Se (50 mmol), respectively, was dissolved in TOP (25 mL) at an elevated temperature.

Synthesis of red-light-emitting CdSe/$Cd_{1-x}Zn_xS$ QDs: All reactions were conducted in an inert atmosphere using Schlenk techniques. In a typical synthesis of CdSe/$Cd_{1-x}Zn_xS$ QDs, a mixture of CdO (1 mmol), MA (3 mmol), and ODE (15 mL) was degassed in a flask at 110 °C under vacuum. After degassing, the flask was backfilled with Ar, and the temperature was raised to 270 °C. Then, TOPSe (0.5 mmol) was rapidly injected into the flask to promote the nucleation of CdSe cores. After 3 min, the flask was charged with the $Zn(OA)_2$ solution (4 mL), and DDT (1.5 mmol) was dropwise added to grow the $Cd_{1-x}Zn_xS$ shell. After 30 min, $Cd(OA)_2$, $Zn(OA)_2$, and TOPS were repeatedly injected for the additional growth of the $Cd_{1-x}Zn_xS$ shell to achieve a total shell thickness of 4.5 nm. The synthesized CdSe/$Cd_{1-x}Zn_xS$ QDs were repeatedly purified by a typical precipitation/ redispersion method.

Surface ligand modification of the QDs: The as-synthesized $CdSe/Cd_{1-x}Zn_xS$ QDs were precipitated by adding ethyl alcohol (5 ml). Then, the precipitated QDs were redispersed in chlorobenzene (2 ml). Thereafter, octylamine (1 ml) was added in QD solution to replace the oleic acid ligands with octylamine ligands. After 8 h of mixing, the QDs were precipitated again by adding ethyl alcohol to remove impurities during ligand modification. The modified QDs with octylamine ligands were dissolved in chlorobenzene.

2.2 Device Characterization of Thin Film Transistor

2.2.1 Characterization for Thin Film Transistor

Figure 2.1 shows the typical structure of TFTs with three terminals (Gate, Source, Drain). All the electrical characterizations were measured with a semiconductor parameter Analyzer (Agilent 4156C) in ambient air. Transfer characteristics were obtained in a linear regime at drain-to-source voltage (V_{DS}). V_{th} was determined at the value of the x-axis intercept of linear extrapolation of the I_{DS}–V_{GS} curve. Field-effect mobility was calculated from $\mu_{FE} = \{L/(WV_{DS}C_{OX})\} \times (\partial I_{DS}/\partial V_{GS})$. The thickness and surface roughness of active layer were measured by the atomic force microscopy (AFM, Bruker, MULTIMODE-8-AM). Raman spectrometer (WITEC alpha300) was used to analyze the Raman spectra of SWNTs electrodes and $MoTe_2$ flakes with a 532 nm laser excitation and 1 μm of beam size. XPS was investigated by PHI 5000 Versa Probe II (ULVAC-PHI) at 10^{-7} Pa.

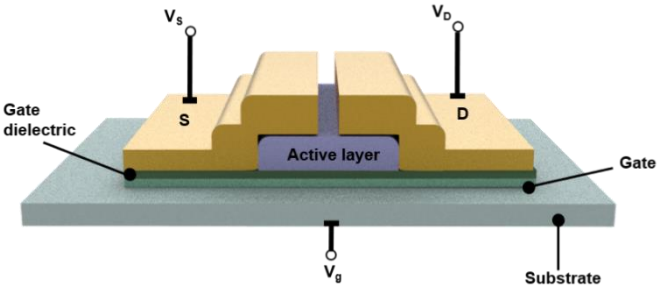

Figure 2.1 An example of typical device structure in thin film transistor.

2.2.2 Characterization of light response

Light for photo response was illuminated by the Multi-Wavelength Fiber-Coupled LED source (Mightex, Inc.) with various wavelength from NIR to UV (365 nm, 455 nm, 530 nm, 656 nm, 740 nm, 850 nm, 940 nm) and 3 mW cm^{-2} of power density.

2.3 Device Characterization of Quantum Dot Light-Emitting Diode

2.3.1 Current-voltage-luminance Measurement of QLEDs

The current-voltage (I-V) characteristics were measured with a Keithley 236 source measurement unit, while the electroluminescence was measured with a calibrated Si photodiode (Hamamatsu, S5227-1010BQ) with a size of 10 mm × 10 mm placed at an angle normal to the device surface, assuming that the device was a

Lambertian source. To detect a turn-on voltage of light-emitting diodes, we use an ARC PD438 photomultiplier tube (PMT) with the Keithley 236 source measurement unit. The electroluminescence (EL) spectra and the Commission Internationale de L'Eclairage (CIE) color coordinates were measured with a Konica-Minolta CS-1000A spectroradiometer. The luminance and efficiency were calculated from the photocurrent signal of photodiode with a Keithley 2000 multimeter and corrected precisely with the luminance from spectroradiometer (CS-2000).

The chromatic characteristics were calculated from EL spectra measured by the CS-1000A spectrometer using the CIE 1931 color expression system. The tristimulus values XYZ can be calculated by following equations,

$$X = K_m \int_0^\infty \bar{x}(\lambda)P(\lambda)d\lambda \tag{2.1}$$

$$Y = K_m \int_0^\infty \bar{y}(\lambda)P(\lambda)d\lambda \tag{2.2}$$

$$Z = K_m \int_0^\infty \bar{z}(\lambda)P(\lambda)d\lambda \tag{2.3}$$

where, P(λ) is a given spectral power distribution of emissive source, $\bar{x}$, $\bar{y}$ and $\bar{z}$ are the CIE standard color matching functions (see Figure 2.2) and K_m is the weighing constant (683 lm W^{-1}). From the tristimulus values, the CIE color coordinates were calculated by following equations,

$$x = \frac{X}{X+Y+Z} \tag{2.4}$$

$$y = \frac{Y}{X+Y+Z} \tag{2.5}$$

$$z = \frac{Z}{X+Y+Z} \tag{2.6}$$

Any color can be plotted on the CIE chromaticity diagram.

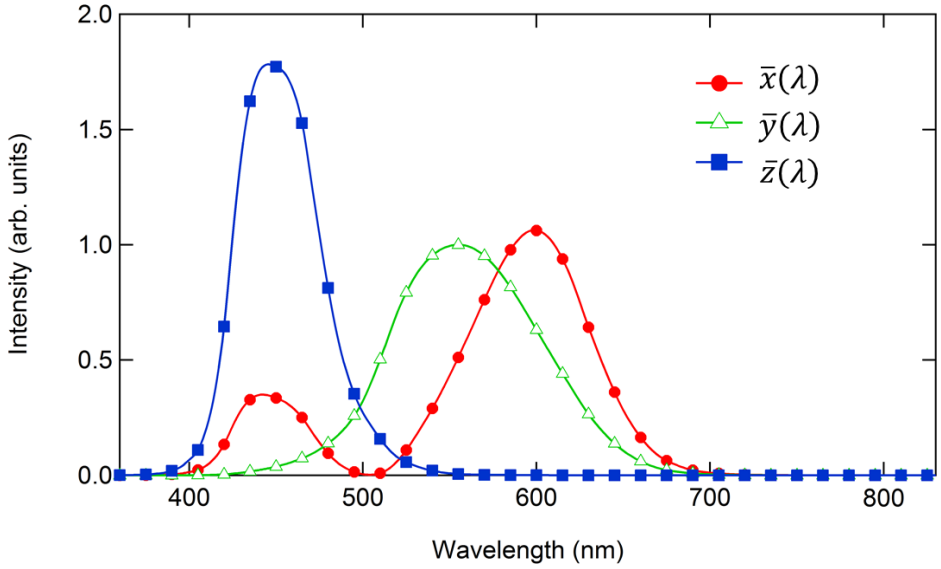

Figure 2.1 The CIE standard observer color matching functions

2.3.2 Efficiency Calculation Methods

To evaluate the emission properties of light-emitting diodes, the commonly employed efficiencies are the EQE, the current efficiency (C.E.) and the power efficiency (P.E.).

The external quantum efficiency can be defined by the following equation.

$$\mathrm{EQE} = \frac{number\ of\ emitted\ photons}{number\ of\ injected\ electrons}(\%)$$

Typically, QLEDs or OLEDs emit light into the half plane due to the metal contact. Without any modification for increasing out-coupling efficiency, over 80% of the emission can be lost to internal absorption and wave-guiding in a simple planar light-emitting device.

Since human eye has different spectral sensitivity in visible area, the response of the eye is standardized by the CIE in 1924 (see $\bar{y}$ in Figure 2.2). The luminous efficiency weighs all emitted photons according to the photopic response of human eye. The difference is that EQE. weighs all emitted photons equally. C.E. can be expressed by the following equation.

$$\mathrm{C.E.} = \frac{luminance}{current\ density}(cd\ A^{-1})$$

The luminance value (cd m^{-2}) can be easily measured by the commercial luminance meter (CS-1000A in this thesis).

The power efficiency is the ratio of the lumen output to the input electrical power as follows,

$$\mathrm{P.E.} = \frac{luminous\ flux}{electrical\ power}(lm\ W^{-1})$$

The EQEs can be useful to understand the fundamental physics for light emission mechanism, while the PEs can be useful to interpret the power dissipated in a light-emitting device when used in a display application.

2.3.3 Other Characterization Methods

UV-Visible Spectroscopy: The transmission and absorption spectra were measured with U-2900 (Hitachi) UV-Visible Scanning Spectrophotometer. In case of solution, materials were dissolved in toluene or chlorobenzene. For the film measurement, materials were spin-coated or evaporated thermally in the thickness of ~50 nm on quartz substrate. The reflectance spectra were also measured by U-2900 spectrophotometer. The average transmittance (T_{avg}) was calculated by the following equation.

$$T_{\mathrm{avg}} = \frac{\int_{\lambda_1}^{\lambda_2} T(\lambda)\mathrm{d}\lambda}{\lambda_2 - \lambda_1} \tag{2.7}$$

Where $T(\lambda)$ is the transmittance as a function of the wavelength, T_{avg} was usually calculated by integrating $T(\lambda)$ from 400 nm (λ_1) to 800 nm (λ_2).

Ultraviolet Photoelectron Spectroscopy (UPS): The UPS spectra were performed using Kratos AXIS-NOVA, employing He I light source and a hemispherical analyzer. The valence band maximum (VBM) of the nanocrystals was calculated using the following equation.

$$VBM = 21.2\ eV - \left|E_{cutoff} - E_{onset}\right| \tag{2.8}$$

The conduction band minimum (CBM) value was obtained by using the VBM and the excitonic band gaps of QDs, estimated from the PL spectra of QDs.

Film Thickness Measurement: Ellipsometers (L2W15S830 with 632.8-nm He-Ne laser light, Gaertner Scientific Corp. and M2000D, Woollam) and an AFM (XE-100, Park Systems) were used for measuring the thickness of films

Transmission electron microscopy (TEM): The TEM images of the QDs were obtained using a JEM-2100F at 200 KeV to analyze their average size and size distribution. The energy dispersive x-ray (EDX) spectra of QDs were acquired through Si-Li attached on main body of TEM. Low-coverage samples were prepared by placing a drop of a dilute toluene dispersion of QDs on a copper grid (300 mesh) coated with an amorphous carbon film. The composition of QDs was measured with inductively coupled plasma optical emission spectroscopy (Agilent ICP-OES 720).

Chapter 3

The Study of P-type Oxide Thin Film Transistors

Recently, n-channel oxide semiconductors such as indium-gallium-zinc oxides [3, 4] have been developed to such an extent that they can be applied to commercialized backplanes in flat panel displays such as active-matrix LCD and OLED. However, sluggish progress in the development of p-type oxide semiconductors has impeded the launch of newly envisioned applications [48-51] in which complementary devices and circuits are mandatory for achieving low power consumption, good noise immunity, and simplified-circuit-design-enabled high-density integration.

In this sense, among various p-type oxide semiconductors such as SnO [52], Cu_2O [53], and NiO [54], a recent significant progress in SnO TFTs has enhanced the

possibility of complementary circuits that are fully implemented only by oxide semiconductors, which are attractive for applications of flexible [48, 49], transparent [3, 4, 52], and transient [50, 55] (i.e., physically dissoluble or disintegrated) electronics. However, most of SnO TFTs were predominantly implemented by using conventional high-work function-metals (e.g., Ni, Au, and Pt) [54] as source and drain electrodes. The metal electrodes are not favorable for the afore-mentioned applications which are required to have either type of properties such as easy bendability, stretchability, and physical disintegration. Thus, for the future electronics based on SnO TFTs, intensive and systematic studies on alternative electrodes based on nanowire structures other than metal electrodes have been highly anticipated [46, 57]. Interestingly, SnO TFTs with alternative electrodes such as AgNW, graphene, poly(3,4-ethylenedioxythiophene): poly(styrenesulfonate) (PEDOT:PSS), and carbon nanotubes have not been reported yet, compared with several reports [48, 51, 56] on n-type oxide TFTs with flexible electrodes. Among alternative electrodes for SnO TFTs, single walled carbon nanotubes (SWNTs) are one of promising candidates because of excellent adaptability for the stretchable and transparent electronics due to low bending strains, durable transparency, excellent reliability associated with excellent electrical and thermal conductivity, etc.

In this study, for the emerging novel electronic applications, we proposed to use the spray-coated SWNTs for SnO TFTs as alternative electrodes of a source and a drain. Furthermore, by analyzing current–voltage characteristics of the implemented SnO TFTs depending on substrate temperature, we systematically investigated the intrinsic field effect mobility as well as electrical contact properties for SnO TFTs in order to understand (or validate) feasible electrical properties of spray-coated SWNTs with SnO films, compared to the conventional metal electrodes.

3.1 Device Fabrication of SnO TFTs with Spray-Coated Single walled Carbon Nanotubes as S/D Electrodes

Figure 3.1(a) shows a schematic view of the proposed SnO TFTs, adopted with an etch-stopped layer of SU-8 dielectric and single-walled carbon nanotubes as source and drain electrodes. These were prepared by spray-coating the SWNTs (Turball Ink; OCSiAl Asia Pacific) [57]. An n-type silicon wafer (ρ ~ 0.005 ohm cm) with thermal oxide (~18 nm) was used as a starting substrate, playing the role of gate electrode. This was followed by the deposition of SnO (10 nm) by RF magnetron sputtering in a mixed gas (~Ar/O_2) without heating of the substrate [58]. The immediate lift-off process in the acetone forms the defined area of SnO as an active layer. Next, the SU-8 was photo-lithographically patterned as an etch stop layer and channel passivation layer. Thereafter, single-walled carbon nanotubes were spray-coated entirely over the sample on a hot plate at 110ºC, and the SWNTs were removed from the periphery with reactive ion etching through photolithographic patterning, thus forming S/D electrodes.

Figure 3.1(b) shows surface images of the SWNTs as analyzed by a scanning electron microscope (SEM). The analysis indicates that all SWNTs were densely entangled, forming 100-nm-thick SWNT films as source and drain electrodes. For a reliable characterization of SnO TFTs with SWNT electrodes, PMMA (9 wt% solution in toluene) was spun on SnO TFTs and baked at 110 ºC for 12 h for an isolation of moisture and oxygen in air by encapsulation [59].

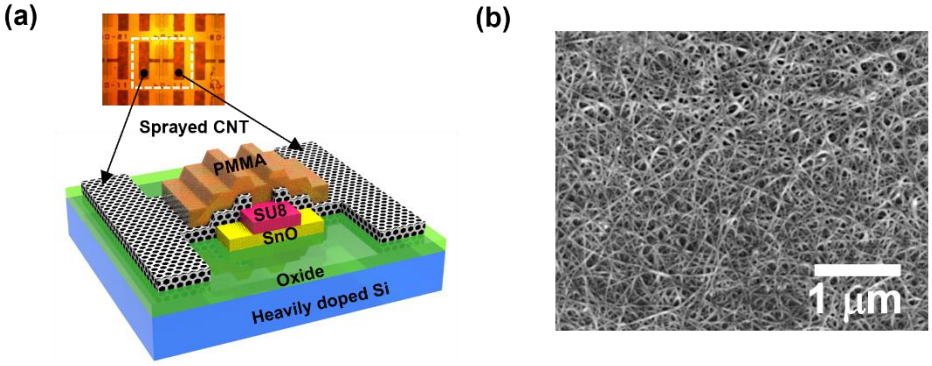

Figure 3.1 Schematic with optical image for (a) SnO field-effect transistors with spray-coated carbon nanotube electrodes as source and drain, encapsulated with PMMA (b) SEM images of spray-coated SWNTs, forming source and drain electrodes.

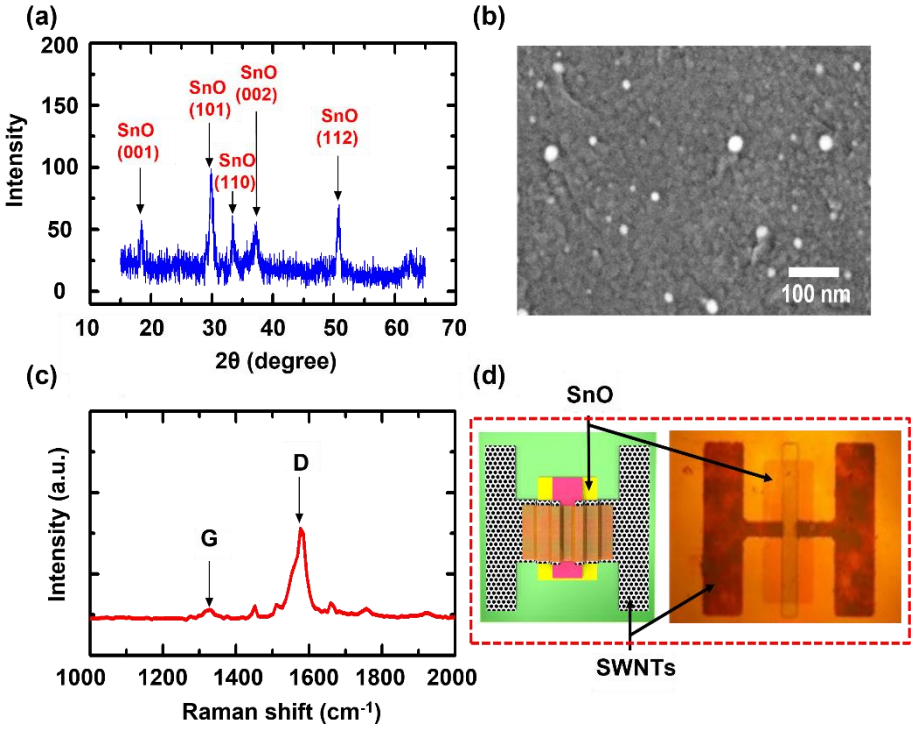

Figure 3.2 (a) High intense XRD lattice planes and (b) SEM images for SnO film prepared by sputtering. (c) Raman spectra of spray-coated SWNTs in the region of source and drain electrodes as shown in Fig. 3.2(d). (d) Top views of schematics and optical microscope images for the implemented SnO TFTs with spray coated SnO TFTs.

After implementation of SnO TFTs, crystallographic information of SnO was confirmed by x-ray diffraction (XRD; Rigaku, high-resolution XRD) analysis in Fig. 3.2(a), (b). Also, SWNTs peak after spray-coating were analyzed by Raman analysis (excitation wavelength ~ 532 nm, Witech alpha 300) in Fig. 3.2(c), (d). In addition, direct probing on SWNTs as electrodes was used for electrical characterization. To investigate the contact and channel properties of SnO TFTs with spray-coated SWNT electrodes, all electrical properties (Keithely 4200 A) of the SnO TFTs were evaluated

in air and a vacuum with a change in substrate temperature ranging from 150 to 333 K. In this work, the low temperature was achieved in the cryo-probe station (model: M6VC, MStech. co) by using liquid nitrogen-based cooling down.

3.2 Electrical Performance of SnO TFTs

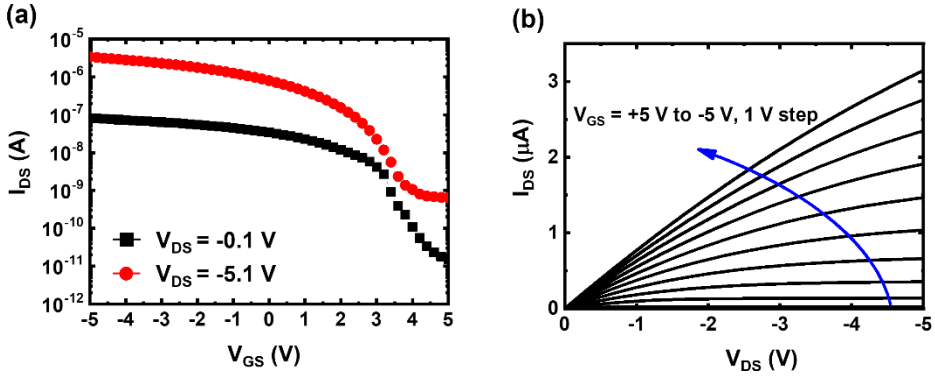

Figure 3.3 (a) Representative transfer characteristics of SnO TFTs in linear (V_{DS} = -0.1 V) and saturation regimes (V_{DS} = -5.1 V). (b) Output characteristics of SnO TFTs as gate-to source voltage decreases in steps of -1 V. Channel length (L) and width (W) for TFTs were 40 μm and 30 μm, respectively.

Figure 3.3(a) shows the transfer characteristics of SnO TFTs as a drain to source bias (V_{DS}) decreases, ranging from −0.1 and −5.1 V. In this study, field effect mobility (μ_{eff}) was extracted from conventional current–voltage (*I–V*) equation for both a linear and a saturation regime. The threshold voltage was extracted by transconductance (g_m) method in the linear regime. In the linear regime, electrical parameters for SnO TFTs were extracted as a threshold voltage (V_{th}) of 3.0 V, a subthreshold swing (SS) of 0.4 V dec^{-1}, a field effect mobility (μ_{eff}) of 0.69 cm^2 V^{-1} s^{-1}, and a current on/off ratio (I_{on}/I_{off}) of 4.2×10^3. On the other hand, in the saturation regime, V_{th} decreased from 3 to 1.3 V, whereas the SS (~0.6 V dec^{-1}), μ_{eff} (~0.70 cm^2 V^{-1} s^{-1}), and I_{on}/I_{off} (~3.5×10^3) were determined to be similar values within experimental error ranges. In addition, as shown in Fig. 3.3(a), the off-leakage current

was slightly increased as V_{DS} decreases gradually from −0.1 to −5.1 V. In consideration of physical dimension of channel length and temperature dependency of leakage current, the origin of mechanism for leakage current might be ascribed to the back-channel conduction or/and gate induced drain leakage in this study in lieu of drain induced barrier lowering (DIBL). Typically, DIBL can be observed for the short channel devices with channel length less than several micrometers. However, for this device as shown in Fig. 3.3(a), the channel length is 35 μm. Therefore, in this dimension, it is not feasible to speculate that the leakage increase is coming from the physics of DIBL. In addition, Fig. 3.4(b) shows that as V_{DS} decreases from −0.1 to −5.1 V, the increase of a leakage current was observed even for the long channel device with a channel length of 95 μm. Therefore, the drain leakage in this study might be came from other transport mechanisms. In addition, as another evidence, as shown in Fig. 3.5, the leakage current level also increases as the temperature increases.

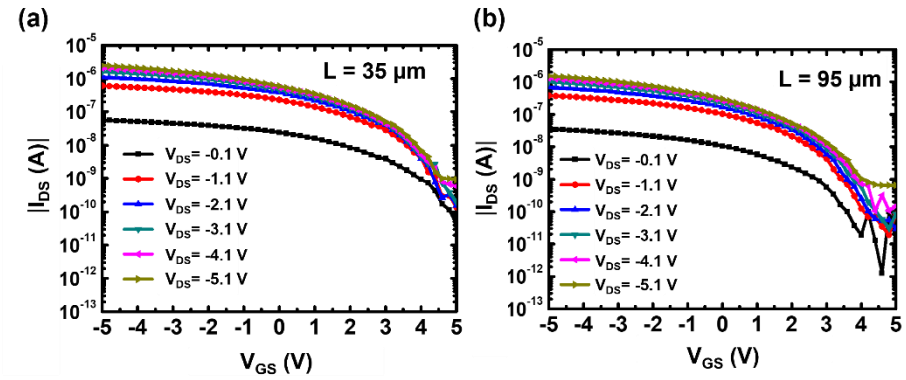

Figure 3.4 Channel length dependency on leakage current for SnO TFTs with (a) L= 35 μm, and (b) L= 95 μm at room temperature as the drain bias decreases from -0.1 V to -5.1 V.

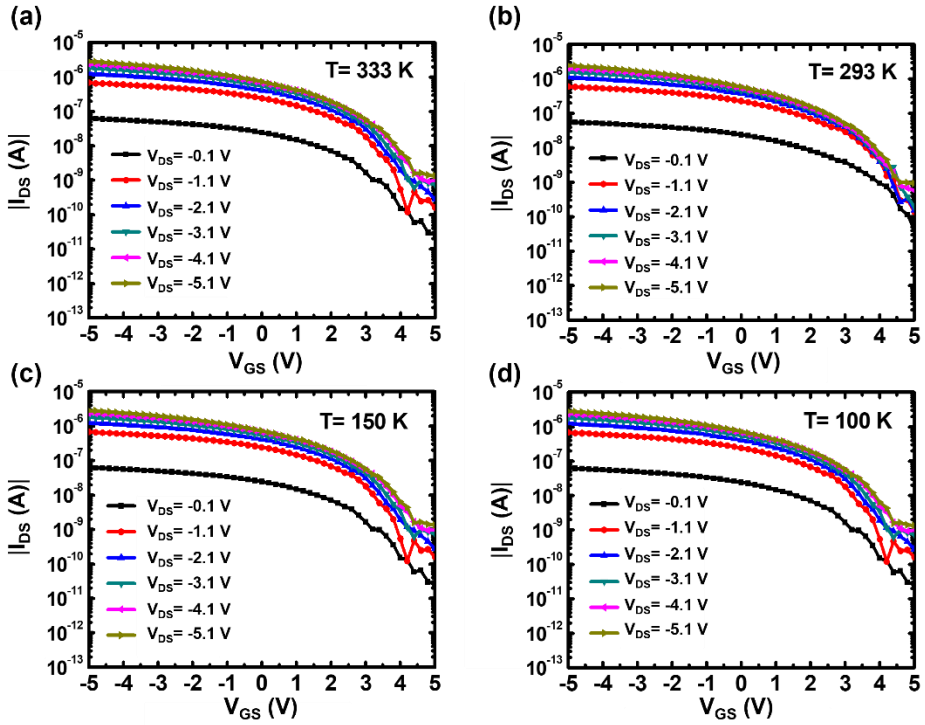

Figure 3.5 Transfer characteristics for SnO TFTs with channel length of 35 μm depending on the drain bias ranging from -0.1V to -5.1 V as substrate temperature decreases from T=333 K to 100 K.

In this sense, the trend of leakage current increase, observed as the drain bias increases, is not possibly due to the barrier height of lowering associated with drain bias, typically speculated as the origin of physics of DIBL phenomena. It was reported that DIBL is not related with temperature dependency, thereby this behavior is not mainly coming from DIBL.

Figure 3.3(b) shows that typical modulation and good saturation behaviors for a drain-to-source current (I_{DS}) were observed as the gate-to source voltage (V_{GS}) varied from 5 to −5 V with a voltage step of −1 V and a change in the V_{DS} of less than −5 V.

3.3 Contact Resistance of Spray-coated SWNTs as S/D Electrodes

For an analytical investigation of the electrical contact properties of SnO TFTs with spray-coated SWNTs as electrodes, a gated transfer length method (TLM) was employed for the SnO TFTs. The transfer characteristics of SnO TFTs variations in their channel lengths ranging from 35 μm to 95 μm were characterized at a drain-to-source bias of -0.1 V in the linear regime in air at room temperature. For further analysis of the contact resistance during changes in temperature, the same measurement was performed in a vacuum chamber with a base pressure of 10^{-6} Torr as the substrate temperature changed from 150 K to 333 K.

At room temperature, the transfer characteristics in air were similar to those in a vacuum. This indicated that the electrical properties were negligibly changed in a vacuum owing to PMMA encapsulation. Fig. 3.6 (a) shows the representative transfer characteristics measured at room temperature with a change in channel length from 35 μm to 95 μm. Figure 3.6(b) shows the width normalized overall resistance of ($W \cdot R_{on}$) at T = 293 K with a change in the gate-to-source bias ranging from -2 V to -5 V. It can be expressed as the sum of the channel resistance ($r_{ch}L$) and contact resistance ($2R_{S/D}$) according to

$$R_{on} = \left.\frac{\partial V_{DS}}{\partial I_{DS}}\right|_{V_{DS}\to 0}^{V_{GS}} = r_{ch}L + 2R_{S/D} = \frac{L}{W\mu_{FEi}C_G(V_{GS} - V_{Ti})} + 2R_{S/D} \tag{1}$$

where r_{ch} is the channel resistance per channel length (L) unit, and $2R_{S/D}$ is the combined contact resistance ($R_{S/D}$) associated with the source and drain electrodes. Here, μ_{FEi} and V_{Ti} are the intrinsic field effect mobility and threshold voltage, respectively. The contact resistance [60] ($2R_{S/D}$) and the unit channel resistance (r_{ch})

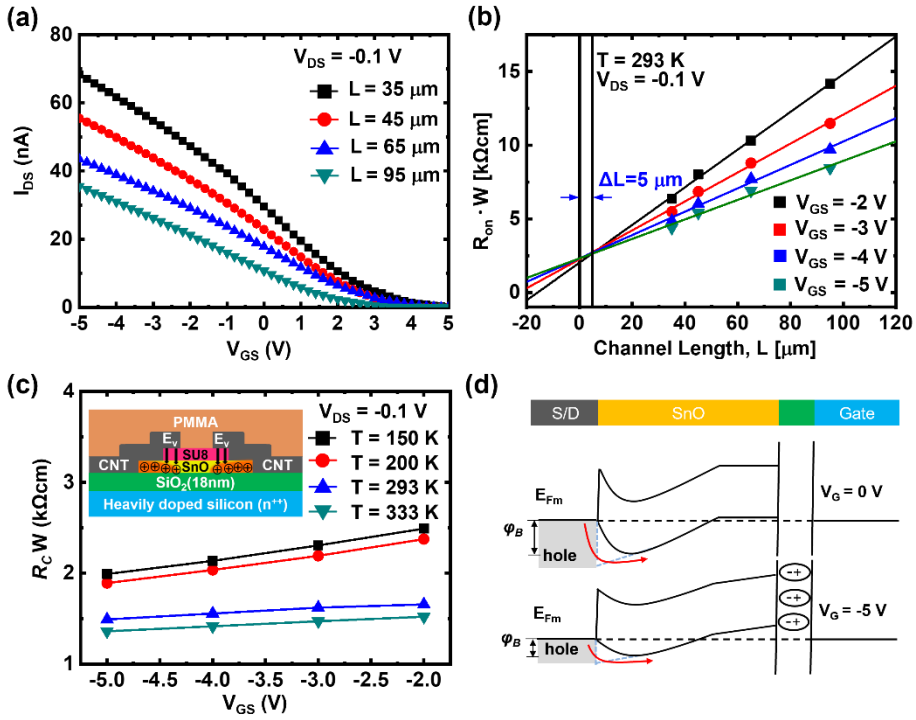

Figure 3.6 (a) Transfer characteristics of SnO TFTs with spray-coated carbon nanotube electrodes at different channel lengths ranging from 35 to 95 μm. (b) Width normalized device resistance as a function of channel length at gate voltages ranging from −2 V to −5 V, extracted from measured *I*–*V* characteristics in figure 3(a). (c) Width normalized contact resistance extracted as temperature varies from T= 150 K to 333 K. Inset denotes electric-field-induced charge profile in the channel, coming from electric field in region at top of etch stop later of SU-8. (d) Schematic diagrams that denote formation of Schottky barrier at interface between metal electrode and SnO semiconductor for either zero bias or negative bias.

can be extracted from the intercept and slope, respectively, of linear fits to plots of $R_{on} \cdot W$ as a function of L for different gate voltages, as shown in Fig. 3.6(b).

Fig. 3.6(b) shows that the normalized resistance curves merge at a channel length value of L_o, which is the independent gate voltage. L_o can be understood as an additional channel length that is introduced by the presence of the contact. In this study, L_o was extracted as +5 μm, which indicates that the effective channel length (L_{eff}), governed by the relationship of $L_{eff}(V_{GS}) = L_{draw} - \Delta L(V_{GS})$, decreases. As shown in the inset of Fig. 3.6(c), this hints that the hole accumulation layer directly below an etch stop layer results in a reduction of the effective channel length. This is similar to the behavior in MOSFETs with lightly doped drain (LDD) structures [61]. However, effective channel width increment and associated 3D effects are expected to be minor due to negligible gate overlap and active patterning process during SnO deposition.

The external contact resistance was extracted using the same method [61] reported for LDD structures. All contact resistance values depending on V_{GS} and temperature are plotted in Fig. 3.6(c). All devices indicate that the extracted gate voltage with changes in gate bias consistently decreased as the gate bias was changed from −2 V to −5 V.

At room temperature, the contact resistance (~1.49 kΩ·cm) for SnO TFTs, adopted with SWNT electrodes in this work, is comparable to or better than that of conventional Ni electrodes (~14 kΩcm) [68]. In addition, global electrical properties for SWNTs are expected to have high conductivity like metal films due to the very small percolation threshold which results from the entangled shape of SWNTs composed of heterogeneous (i.e., the typical ratio of a metallic to a semiconducting

SWNTs is 1 to 2) and multilayered SWNTs [69]. Thus, this behavior, in the present works, might be less affected by diameter and chirality distribution of SWNTs. Furthermore, the extracted contact resistance increased as the temperature was reduced, indicating that the carrier injection barrier (φ_B) between SnO and the spray-coated SWNTs ($\phi_{SWNT} \sim 5.05$ eV, work function [62]) increased owing to thermionic emission theory, which can be represented [63] as

$$r_c = \frac{A}{T}\exp\left(\frac{q\varphi_B}{kT}\right), \tag{2}$$

where A is a temperature-independent pre-factor parameter, φ_B is the height of the SWNT-SnO barrier, and k is the Boltzmann constant.

By using Schottky–Mott theory [64], Schottky barrier ($e\varphi_B$) was estimated to be 0.75 eV by the ideal Schottky barrier relation; $e\varphi_B$= VBM(SnO) − ϕ_{SWNT}, where valence band maximum (VBM) [65] for SnO is ~5.8 eV. In addition, the bulk transport in the vertical direction contributes the increase in series resistance as the temperature decreases owing to the exponential decay of the field effect mobility versus temperature. Furthermore, the width normalized contact resistance value at T=150 K increased twice as much as that of the SnO TFTs at T=333 K. All properties reasonably matched the data in the literature [58] reported previously. In addition, for a better understanding of contact resistance behaviors, the band diagrams, as described in Fig. 3.6(d), predicted that the Schottky barrier between SnO and spray-coated SWNTs would decrease. Thus, the parasitic contact resistance was reduced when a negative gate bias was applied, compared with that of SnO TFTs with zero gate bias.

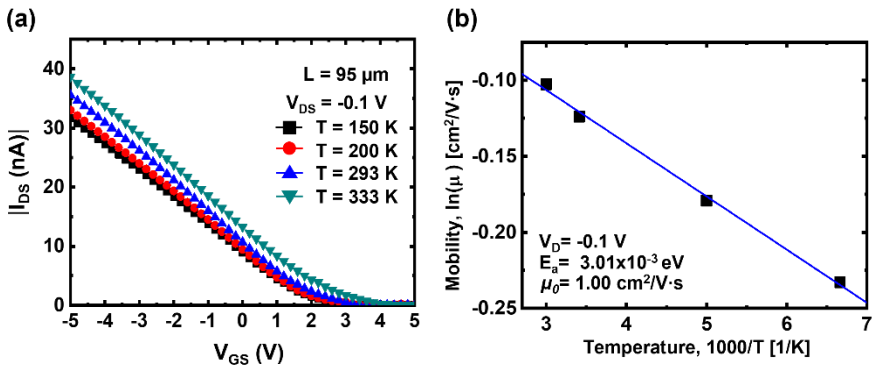

Figure 3.7 (a) Transfer characteristics of SnO TFTs with spray-coated carbon nanotube electrodes as substrate temperature changes from 150 K to 333 K. (b) Arrhenius plots of channel field effect mobility obtained from SnO TFTs with spray-coated SWNTs.

In addition to the electrical contract properties, the channel transport of SnO TFTs with spray-coated SWNTs was systematically analyzed by using field effect mobility as the temperature changed from 150 K to 333 K. Figure 3.7(a) shows the transfer characteristics of SnO TFTs with spray-coated SWNTs (W/L = 30/95 μm) as the temperature changed from 150 K to 333 K. At each temperature, the field effect mobility was extracted at a maximum value of transconductance g_m, given by

$$g_m = \left.\frac{\partial I_{DS}}{\partial V_{GS}}\right|_{V_{DS}=constant} = \frac{W}{L} C_{ox} \mu_{eff} V_{DS} \tag{3}$$

where W is the channel width, L is the length, C_{ox} is the oxide capacitance, μ_{eff} is the field effect mobility, and V_{DS} is the drain-to-source bias. The field effect mobility for a long channel device was extracted as the temperature was increased

from 150 K to 333 K. The investigation of activation energy for field effect mobility (μ_{eff}) is based on the consequence of assuming a multiple trapping and release (MTR) model with an exponential distribution of trap states, which is known as the Meyer–Neldel Rule (MNR) [66]. Therefore, the field effect mobility (μ_{eff}) is given by a relation with

$$\mu_{FEi} = \mu_o \exp\left(-\frac{E_A - E_V}{kT}\right) = \mu_o \exp\left(-\frac{E_a}{kT}\right) \tag{4}$$

where E_A - E_V = E_a is the width of the valence band tails. Thus, we plotted the extracted field effect mobilities vs. an inverse of the temperature, as shown in Fig. 3.7(b). The activation energy (E_a) is approximately extracted as 3.01×10^{-3} eV. This indicates that the width of the valence band tails is less than 0.1 eV, which is interpreted as good channel material in a fully accumulated hole channel regime. In this sense, the extraction of activation energy, in the strong accumulation mode at the temperature larger than 100 K, can be valid, thereby yielding a meaningful analysis on the behaviors of conduction of holes in SnO film. Furthermore, as shown in figure 3.8(b), the extracted activation energy (3 meV), in the strong accumulation regime at the temperature ranging from 150 to 333 K, is comparable to the value of 14 meV in the previous report [70] within experimental error range (i.e., several meV range). Extracted activation energy was in the range from 1.2 to 74 meV as gate bias increases from −5 to 3V (Figure 3.8). All of extracted activation energies substantiate that all the traps are fully filled, thereby yielding excellent SnO channel properties. Based on above results, our approach exhibits that the SnO did not deteriorate electrically during subsequent processes such as spray-coating, SU-8 etch stop layer formation [67] or etching of SWNT electrodes located in a periphery region.

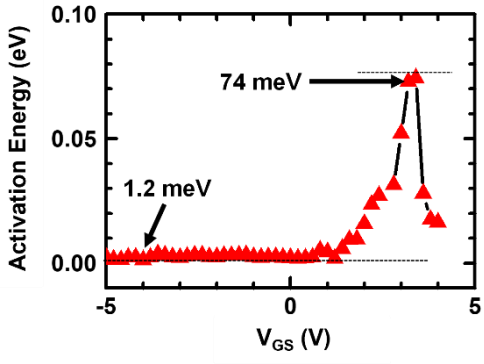

Figure 3.8 Extracted activation energy graph depending on applied gate bias condition.

Table 3.1 Specific and width normalized contact resistance

Electrode materials	Extraction method	Specific contact resistance(R_c) ($\Omega\cdot cm^2$) or width normalized contact resistance ($\Omega\cdot cm$)	Reference
Ni	Transfer length method (TLM)	4.9×10^{-3}	[65]
Mo	Transfer length method (TLM)	5.1×10^{-3}	[65]
Ti	Transfer length method (TLM)	4.9×10^{-2}	[65]
Ni	Gated-Four-Probe Measurements	4.0×10^{-2}	[68]
Ni	Gated-Four-Probe Measurements	~ 14 k$\Omega\cdot$cm	[68] V_{GS}=-14V
SWNT electrodes	Gated TLM Width normalized contact resistance ($R_c\cdot W$)	1.65 k$\Omega\cdot$cm (V_{GS}=-2V) 1.55 k$\Omega\cdot$cm (V_{GS}=-4V) 1.49 k$\Omega\cdot$cm (V_{GS}=-5V)	This work

3.4 Summary

In the present study, as far as we know, SnO TFTs with electrodes as spray-coated SWNTs were implemented for the first time by using 10 nm thick SnO layers, SU-8 etch stop layers, and PMMA passivation. Decent electrical contact properties for the SnO TFTs, comparable to Ni electrodes, were observed (see table 3.1). All electrical properties demonstrated that the oxygen doping and scavenging (i.e., H_2O) effects of PMMA encapsulation partially improved the device contact and reliabilities in terms of electrical contact effects. Furthermore, SU-8 etching stop layer structures are regarded as good etch stopping layers for the perseverance of the SnO layer during the SWNT etching process. Effective channel length reduction behaviors were observed and analyzed by using gated TLM methods. The channel field effect mobility and its activation energy indicate that all electrical properties are nicely preserved during these processes. Beyond electrical performance, SnO TFTs with SWNT electrodes have distinctive merits such as flexibility, transparency, and comparable contact resistance of conventional metals. This means that the device structure is very useful for flexible (or stretchable) device configuration.

Chapter 4

Surface Ligand Modified Quantum Dot Light-Emitting Diodes Controlled by Channel-type Adjustable $MoTe_2$ Thin Film Transistor

Colloidal quantum dots (QDs) based light-emitting diodes (LEDs) have received great attentions due to its high color purity, cost-effective solution processibility, and wide color gamut [32-34, 71, 72]. As compared with organic light-emitting diodes (OLEDs), QDs have been conceived as one of promising light-emitting devices for the next-generation flat panel displays including solid-state lighting [37, 72, 73]. After

first demonstration of quantum dots LEDs (QLEDs), a variety of studies have been actively reported to improve the device performance and operation stability via modulation of variable chemical composition in QDs, optimization of the balance for electron-holes, and adjustment of the device architecture, and others [32, 42, 74, 75].

Furthermore, there have been tremendous research activities to fulfill various aspects which are required for driving of QLEDs in the next generation display panels in terms of material synthesis, [74] brightness, [32] efficiency, [37, 73] long-term stability [76], and others. Nevertheless, a driving transistor which enables to control operation of QLEDs in active-matrixed mode should be considered as one of mandatory elements for the system level demonstration. Among various candidates, low temperature poly silicon (LTPS) or/and oxide semiconductors could be utilized as one of main TFT backplanes for QLEDs [3, 5, 77]. However, a variety of capabilities such as high current drivability, ultra-low power consumption associated with low leakage currents, stability under light illumination environment, and nm scaled-thinness based novel form factors should be secured for the envisioned applications based on QLEDs. As one of possible applications, they are potentially useful for invisible flexible or stretchable displays, and bio-imaging (or sensing) in the implanted bio-medical devices, and light-to-frequency conversion circuits for guaranteeing high-end security issues, and others [12, 78, 79]. In this sense, transition metal dichalcogenides thin film transistors (TMDC-TFTs) could be one of appealing next-generation TFTs to meet the afore-mentioned applications because they have novel material properties including possibility of stacking different layers into functional heterostructures, high on-off ratio, decent field effect mobility, and tunable bandgap depending on number of layers, and absence of dangling bonds [80-83]. Therefore, the platform of TMDC-TFT controlled QLEDs would be attractively applied to display products, which require for rollable, stretchable, multi-functional,

and invisible aspects, and furthermore, TMDCs with ultra-thinness can be potentially extended towards novel applications such as IoT sensors with high security and transient devices which require for zero-waste (or eco-friendliness) and bio-implantable properties [12, 84-87]. However, the in-depth research on validation of a driving capability, which enables to operate QLEDs via TMDC TFTs, has been elusive even though uniqueness of application and its importance for future electronics are significantly high in this field. Until now, there have been very limited reports to address this validation, wherein its feasibility confirmation on the control of QLED-operation via molybdenum disulfide (MoS_2) TFTs was demonstrated, and thereby, type control (e.g., n (or p)-type TFTs) of TFTs and its demonstration on low-power consumption issues were not systematically reported in the work [88]. For the enhancement over the extendibility of span of application and its practical impacts, scheme of ultra-low power consumption in circuits and the in-depth understanding on photo-leakage for TFTs under light-illumination are highly recommended.

In the present work, we aimed not only to fabricate the high performance QLEDs but also to firstly demonstrate the driving capability of multilayered molybdenum ditelluride ($MoTe_2$) TFTs for QLED-operation with an achievement of complementary type transistor based on $MoTe_2$. In order to convert the initial p-type characteristics of $MoTe_2$ to n-type characteristics, amine-based electron donation is utilized by using a Poly-L-lysine (PLL) treatment on the surface of $MoTe_2$ layers. As a result, a successful and clear type conversion of $MoTe_2$ TFTs without degradation of electrical properties was obtained, and both n-type and p-type $MoTe_2$ TFTs demonstrated a stable QLED-operation. In addition, PLL treatment was applied to n-type MoS_2 TFTs in order to induce an improvement of driving currents, which suggests a luminance control of the driven QLEDs. Moreover, fabricated $MoTe_2$ TFTs exhibited excellent suppression of photocurrents under ultraviolet (UV) ~ near-

infrared (NIR) region, showing a unique advantage for the applications such as display backplane transistors as well as light-to-frequency conversion circuits, as compared to other TMDCs and conventional Si materials. This is because a photo-leakage currents should be negligible in display backplane, otherwise it leads to variations of pixel luminance by external illumination during operation or it needs an inevitable addition of blocking layer for penetration of light [89].

In parallel, we investigated the performance improvement of QLEDs itself. Typically, colloidal QDs are capped with bulky acids and long hydrocarbon chain, which enhance a dispersion of QDs in organic solvents to prevent aggregation. Despite these great dispersive properties, organic surface ligands hinder the charge transport between QDs due to low conductivity of capping ligand [39, 40, 90]. To increase the charge transport into QDs, we adopted ligand modification of QDs by replacing long ligands with shorter ligands. From this technique, we could shorten the chain length and lower the injection barrier height between QDs and adjacent layer. As a result, a more balanced charge injection of electron/hole was secured, yielding a greatly increased current efficiency and lifetime of QLEDs. Combined with performance improvement of QLEDs, we highly anticipate these results will contribute to development of emerging QLED applications, which are combined with light-insensitive $MoTe_2$ TFTs. In particular, active-matrixed light-emitting devices, composed of ultra-thin $MoTe_2$ TFTs and highly efficient QLEDs, are highly expected to be utilized for the envisioned applications of bio-medical implanted devices with multi-functional versatility and next generation display technologies.

4.1 Description of QLED display driven by $MoTe_2$ TFTs

Figure 4.1(a) illustrates schematic cartoons for a circuit diagram and visualized device configuration for the light-emitting operation of the QLEDs driven by light-insensitive $MoTe_2$ TFTs. CdSe-based QLEDs, which correspond to a wavelength (~620 nm) of light emission, are connected with multilayered $MoTe_2$ TFTs as driving transistors in series to control the current which is injected toward the light-emitting diodes. With the adoption of well-known scheme as driving TFTs controlled light-emitting diodes, this effectively minimizes the degradation-mediated change in the operating voltage of QLEDs and hence prevents image sticking in display pixels. On-off switching of the light emission in the QLEDs is immediately controlled by the modulation of QLED current (I_{QLED}) which is passed through the channel of the transistor as the gate-to-source voltage for the transistors is switched into the on (or off) operation condition for the driving transistor. With the afore-mentioned scheme, the luminance of QLEDs for red light can be directly controlled by active-matrixed mode which is well-established in FPDs. Furthermore, $MoTe_2$ driving transistors were implemented on the heavily doped Si/SiO_2 (~20 nm) substrate as common-bottom gate configuration after transferring the exfoliated multilayered $MoTe_2$ flakes on the substrate, followed by S/D electrode formation. Detailed conditions for the fabrication of $MoTe_2$ TFTs were described in Fig. 4.2(a). Figure 4.1(b) shows the optical image of fabricated $MoTe_2$ TFTs with a physical dimension (W/L=30/10 μm) of channel width (W) over length (L). In the channel region of $MoTe_2$ layers, a height profile of $MoTe_2$ flake was measured by atomic force microscopy (AFM), which displays 8 nm-thick-$MoTe_2$ flake, corresponding to 12 layers [91]. Thereafter, Figure 4.1(c) shows core/shell structure ($CdSe/Cd_{1-x}Zn_xS$) of QDs based on oleic acid (OA) and octylamine (OcA) ligands.

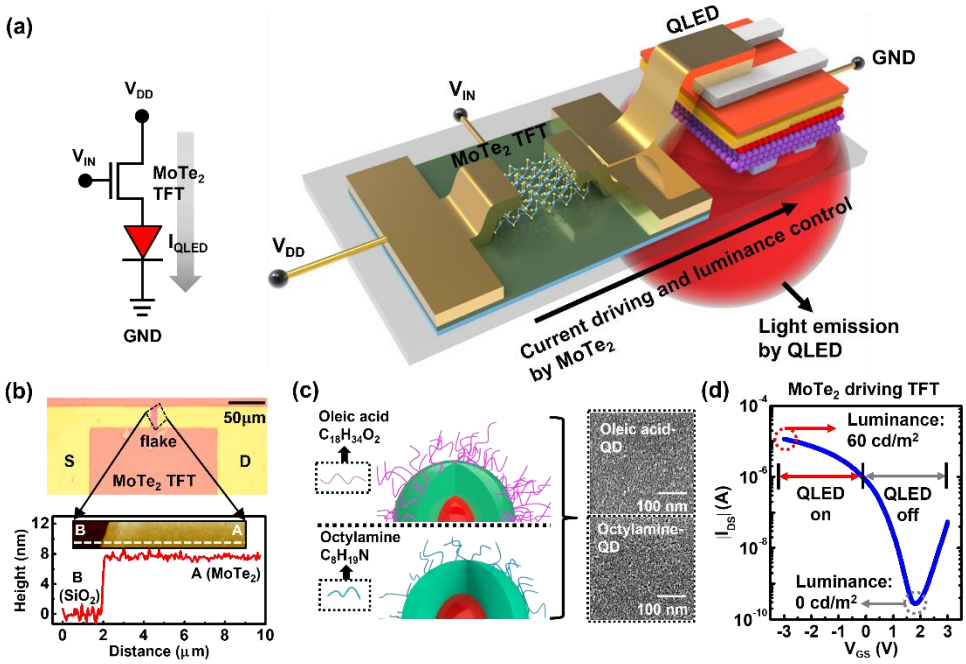

Figure 4.1 (a) Circuit diagram (left) and schematic cartoon (right) for QLED operation driven by $MoTe_2$ TFTs. (b) An optical image of $MoTe_2$ TFT and height profile of multilayered $MoTe_2$ flake measured by AFM. (c) Core/shell structure of QDs based on oleic acid and octylamine ligands, and corresponded SEM images. (d) Transfer characteristics of a fabricated p-type $MoTe_2$ TFT at V_{DS} = – 0.1 V. Luminance of QLEDs depends on the maximum and minimum currents of driving $MoTe_2$ TFTs.

Also, SEM images indicate that the uniform film morphology was achieved in both OA- and OcA-capped QDs. In this study, for the improvement of performance of QLEDs, ligand modification was utilized not only to reduce the insulating property, but also to enhance the chemical bonding strength. Figure 4.1(d) presents the transfer characteristics of p-type $MoTe_2$ driving TFTs. The implemented $MoTe_2$ TFTs have on-off ratio ~ 10^5, subthreshold swing (SS) ~ 0.4 V/dec, and field effect mobility ~

12.7 cm^2/Vs, which indicate the decent electrical performance and capability to operate the QLEDs properly. Moreover, a range of gate voltage for $MoTe_2$ TFTs matched with operating voltage of QLEDs by using 20 nm SiO_2 gate insulator. After $MoTe_2$ TFTs are connected with QLEDs, QLEDs turn on with visible brightness in the on-current region of $MoTe_2$ TFTs larger than "μ" A level currents and turn off in off-current region of $MoTe_2$ TFTs smaller than "μ" A level currents. After the confirmation on device fabrication and electrical characteristics of $MoTe_2$ TFTs, detailed results for ligand modification of QLEDs, type conversion of $MoTe_2$ TFTs, and driving capabilities were demonstrated in following sections.

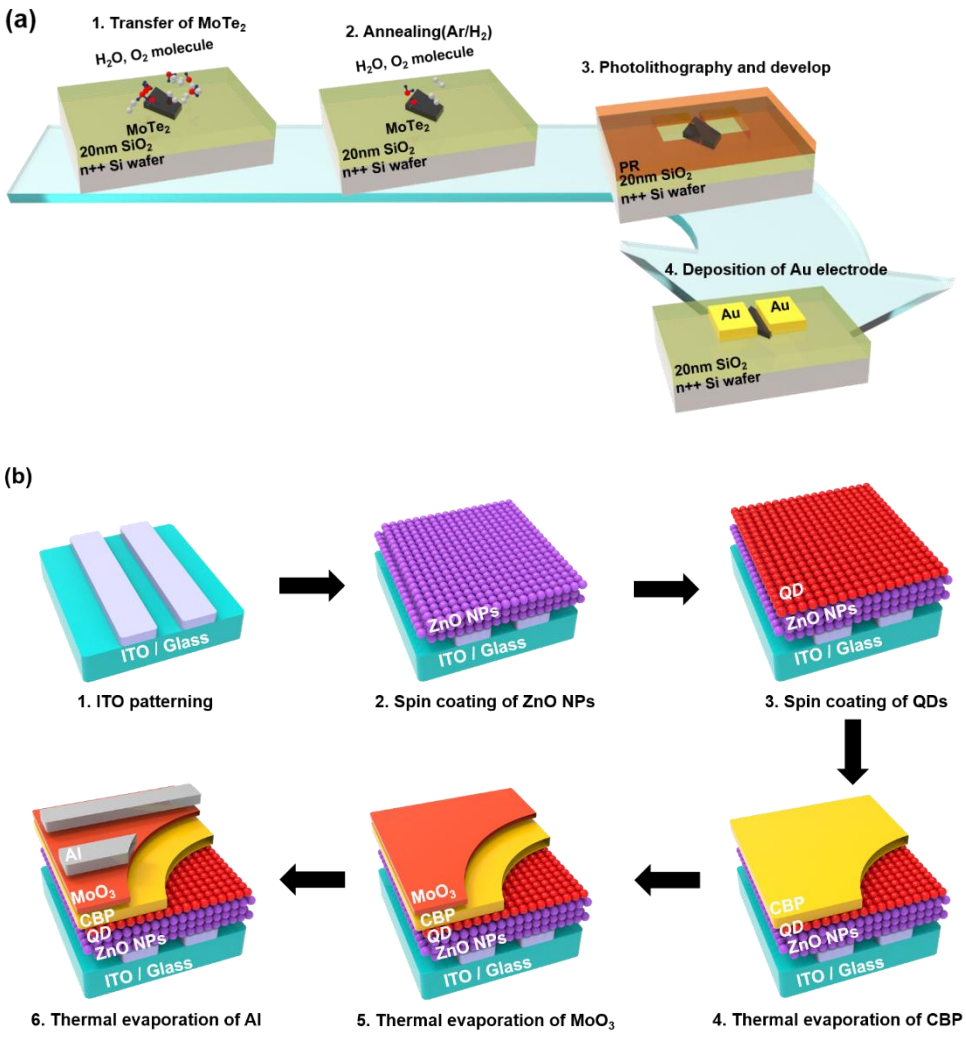

Figure 4.2 (a) Device fabrication process of $MoTe_2$ TFTs with bottom gate structure. Thermal annealing in Ar/H_2 atmosphere was performed firstly after mechanical exfoliation of $MoTe_2$ flakes. Second, conventional lithography and develop were conducted to define S/D. After that, Au electrode was thermally deposited. (b) Device fabrication process of red CdSe inverted QLEDs. ZnO NPs/QDs as ETL/EML were firstly spin coated on the ITO-patterned glass substrate. After that, CBP/MoO_3 as HTL/HIL were thermally evaporated. Lastly, Al as an anode was deposited with a shadow mask.

4.2 Surface Ligand Modification on Inverted Bottom Emissive Quantum Dot Light-Emitting Diodes

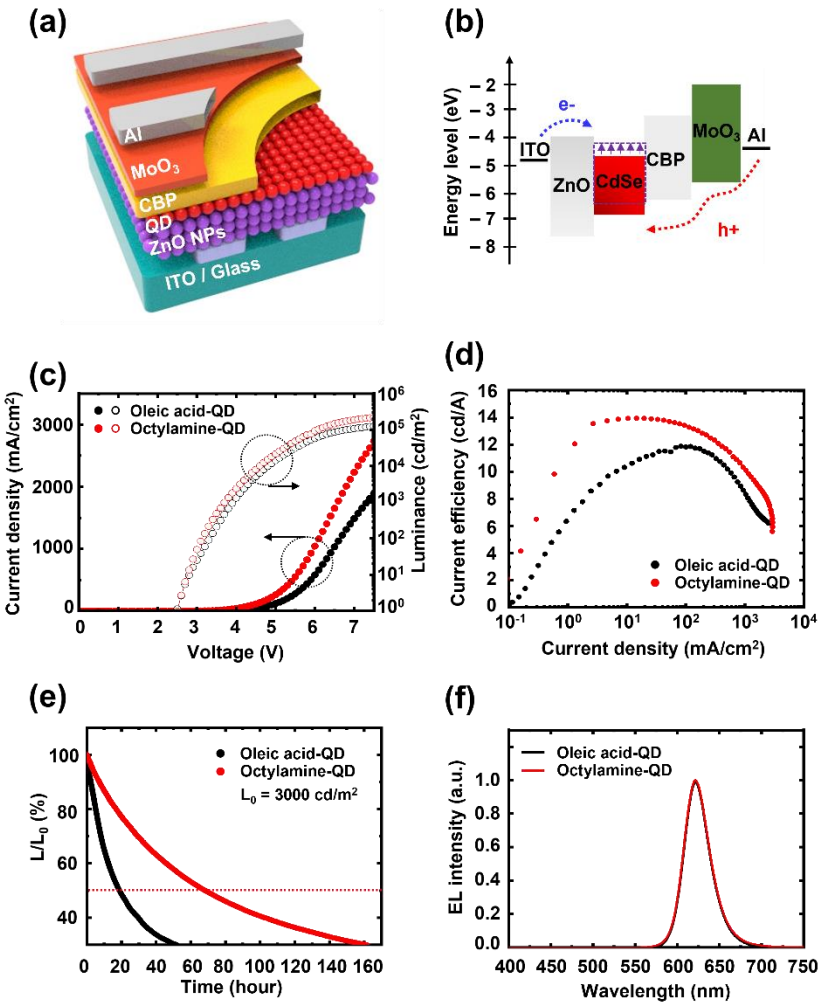

Figure 4.3 (a) Schematic device structure of inverted bottom emitting CdSe QLEDs and (b) Energy level diagram of the device. (c) *J-V-L* characteristics, (d) Current efficiency curves, (e) Operational lifetime characteristics (corresponding to an initial luminance of 3000 cd/m^2), and (f) Normalized EL spectra of QLEDs with OA and OcA ligands.

The operation of the QLEDs display with $MoTe_2$ TFTs begin with the fabrication of an inverted bottom emissive red CdSe QLEDs as the optoelectronic device in Figure 4.3(a). Fabricated QLED devices consist of a ITO/ZnO NPs/QDs/4,4´-bis(9-carbazolyl)-biphenyl) (CBP)/molybdenum oxide (MoO_x)/Al structure as shown in Fig. 4.2(b). In this structure, the light emission of QLED occurs when electrons and holes from ITO/Al electrodes recombine in QDs. Therefore, the electron/hole injection should be balanced to achieve an efficient luminescence. However, as shown in Figure 4.3(b), charge balance of inverted bottom emissive QLEDs is hindered not only by the excessive carrier injection of electron more than that of hole but also by high energy barrier between QD valence band (VB) and highest occupied molecular orbital (HOMO) of hole transport layer (HTL). To resolve the poor electron-hole balance, several attempts have been reported such as inserting an electron blocking layer (EBL) and adopting a Y-doped ZnO NPs as an electron transport layer (ETL) to decrease the electron injection into QDs [92, 93]. However, these strategies cause the device instability in QLEDs. Hence in this study, we utilized a robust ligand exchange strategy to optimize the imbalance of electron/ hole injection and lower the energy barrier between QD and the adjacent layer. In this regard, OA with long ligands, which has been conventionally used for the colloidal stability in organic solvents, was replaced by alternative OcA with shorter ligands in order to minimize the spacing distance between QDs while improving the electronic transport property [43, 94]. The presence of ligand modification with OcA was observed in fourier transport infrared spectroscopy (FTIR), exhibiting the N-H stretching peak at 3200–3500 cm^{-1} in Fig. 4.4.

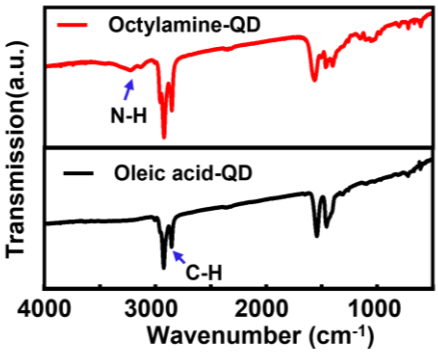

Figure 4.4 FTIR spectra of as-synthesized QDs with oleic acid ligands (lower side) and QDs after ligand modification with octylamine ligands (upper side).

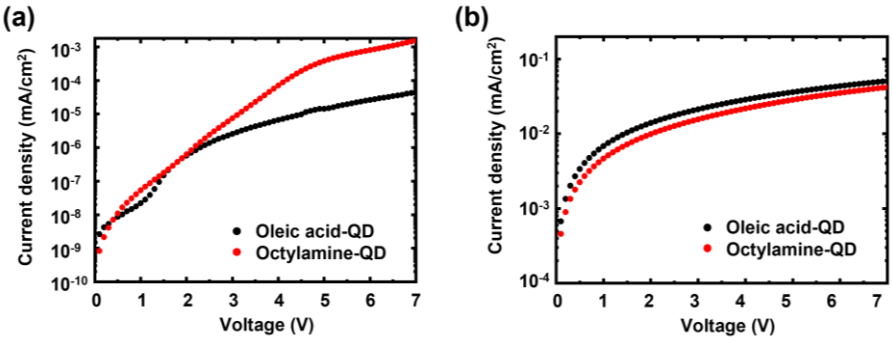

Figure 4.5 *J-V* characteristics of (a) HODs (ITO/PEDOT:PSS/QDs/CBP/MoOx/Al) and (b) EODs (ITO/ZnO NPs/QDs/Al) based on QDs with oleic acid and octylamine ligands.

Moreover, to compare the charge carrier transport behaviors associated with either electron or hole, both EODs and HODs were fabricated in Fig. 4.5. In the HODs, the maximum current of OcA-capped device at the bias condition of 7 V was 15 times higher than that of OA-capped, as compared to the similar electron current level in EODs. This phenomenon is attributed to the energy level upshift of QDs, which was measured by UPS and UV-Visible absorption in Fig. 4.6. Figure 4.3(c) shows the current density–luminance–voltage (*J*–*V*–*L*) characteristics of inverted bottom-emitting CdSe QLEDs with OA and OcA ligands. Due to the improved hole injection property, enhanced current density and luminance for ligand modified QLEDs were observed without change of turn-on voltage. Thereafter, performance index of both QLEDs was evaluated and compared in Fig. 4.3(d), (e). The maximum current efficiency (η_A) and lifetime of OcA-capped QLEDs were 1.2- and 3.7-fold higher than those of OA-capped QLEDs. Herein, the improved current efficiency at low current-density and half-lifetimes (T_{50}) are worthy of attention in terms of the operational stability based on $MoTe_2$ backplane TFTs. In addition, Figure 4.3(f) substantiate the successful ligand modification of QLEDs without any deterioration of quality of light emission and its color. The noticeable performance improvement in QLEDs is fully consistent with all these experimental results, and thereby, manifested by enhancement in terms of current efficiency, lifetime, and energy level shift in the devices. Therefore, the improvement of QLED performance is significantly correlated with efficiently controlled charge balance via ligand modification strategy, which is expected to be indispensable to the future QLED based optoelectronic system. The whole performance of inverted bottom emitting CdSe QLEDs is summarized in Table 4.1.

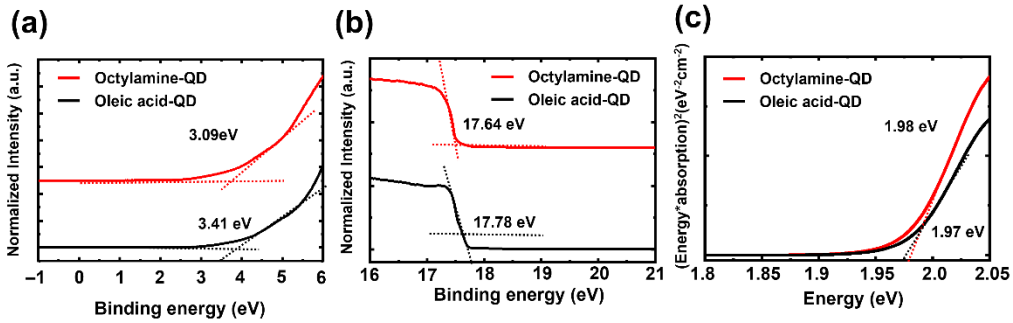

Figure 4.6 UPS spectra at the (a) oneset and (b) cut-off edge dependent on QDs with OA and OcA ligands. (c) Tauc plot of QDs for the band gap.

Table 4.1 Summary of the electrical properties of QLEDs with OA and OcA ligands.

Ligands	λ_{max} (nm)	V_{on} (V)	Luminance$_{max}$ (cd/m^2)	Current efficiency$_{max}$ (cd/A)	EQE$_{max}$ (%)	CIE coordinate (x, y)
OA	623	2.5	144,000	11.8	8.5	(0.68, 0.31)
OcA	623	2.5	175,000	13.9	9.4	(0.68, 0.31)

4.3 Type Conversion of $MoTe_2$ TFTs via Electron-Donated Charge Enhancer

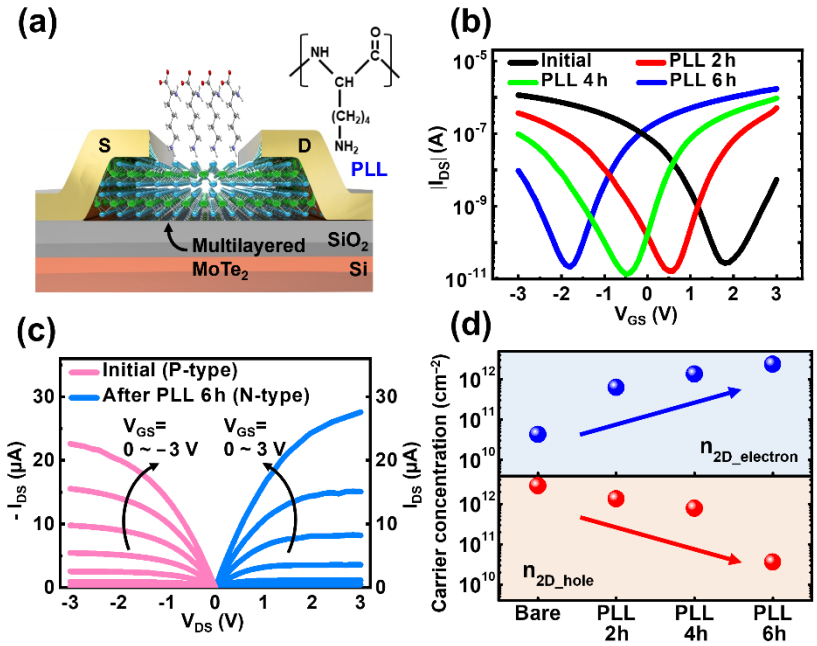

Figure 4.7 (a) A device structure of $MoTe_2$ TFT with PLL treatment. (b) Transfer characteristics of $MoTe_2$ TFTs, which show gradual n-doping effects with multiple PLL treatment. (c) Output characteristics of $MoTe_2$ TFTs before and after 6 hours of PLL treatment. (d) Carrier concentrations of $MoTe_2$ TFTs depending on multiple PLL treatment.

As the most fundamental and important features in electronics, securing both n-type and p-type transistors is an inevitable issue in the most of electrical system to implement complementary circuits due to power consumption and leakage current. In this regard, we realized channel-type conversion of $MoTe_2$ TFTs by using electron-

donated charge enhancer via poly-L-Lysine (PLL) molecular doping. Figure 4.7(a) displays the device structure of $MoTe_2$ TFTs with the PLL treatment, wherein NH_2-based charge transfer can play a role in donating electrons to $MoTe_2$ layers, leading to donor-like doping effects [95, 96]. Figure 4.7(b) shows transfer characteristics of $MoTe_2$ TFTs, corresponding to multiple treatment of PLL with treated time variation up to 6 h, in order to accomplish systematic doping control. Through the split condition for dipping time of PLL solution, well-controlled n-type doping, and systematic threshold voltage (V_{th}) shift were obtained in Fig. 4.7(b). Furthermore, the electrical properties of $MoTe_2$ TFTs seem negligibly changed, and thereby, well sustainable electrical performances except threshold voltage (V_{th}) are observed during multiple treatment of PLL, which indicates clear and stable n-doping process without a degradation of film quality of $MoTe_2$. To confirm the preservation of electrical properties of $MoTe_2$ TFTs, the SS, V_{th}, field effect mobility, hysteresis gap, and current on-off ratio were extracted in Table 4.2, showing improved performances. Thereafter, output characteristics of both p-type and n-type $MoTe_2$ TFTs were measured as shown in Fig. 4.7(c). Initial p-type $MoTe_2$ TFTs exhibit increase of drain currents as V_{GS} negatively increases. On the contrary, $MoTe_2$ TFTs after PLL treatment for 6 h show increase of drain currents as V_{GS} positively increases with slightly enhanced maximum currents. In addition, for quantitative analysis of doping effects, the carrier concentration (n_{2D}) was estimated according to equation (1).

$$n_{2D} = \frac{I_{DS} L}{q_e W \mu V_{DS}} \tag{1}$$

, where I_{DS} is drain-to-source current, L and W are the channel length and width (10/30 μm), q_e is the electron charge, and μ is the mobility. As the treatment time of PLL for

$MoTe_2$ TFTs is augmented, carrier concentration of electron gradually increases from 4.3×10^{10} cm^{-2} to 2.4×10^{12} cm^{-2} and carrier concentration of hole is reduced from 2.8×10^{12} cm^{-2} to 3.6×10^{10} cm^{-2} in 4.7(d). This result clearly elucidates the conversion of carrier type in $MoTe_2$ TFTs.

Table 5.2 Electrical properties of $MoTe_2$ TFTs before and after type conversion.

	SS (V/dec)	V_{th} (V)	Mobility (cm^2/Vs)	Hysteresis (V)	On/off ratio
P-type	0.38	0.2	12.7	0.7	7.94×10^4
N-type	0.34	-0.3	22.5	0.4	8.19×10^4

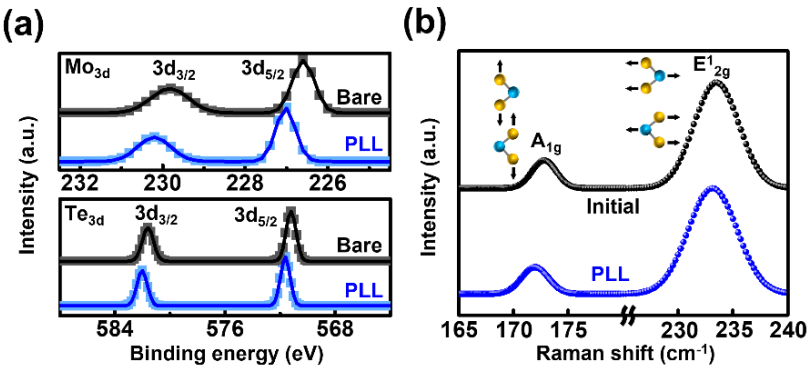

Figure 4.8 Evolution of (a) XPS spectra and (b) Raman spectra for MoTe2 flake before and after 6 hours of PLL treatment.

After confirmation of stable n-doping for the $MoTe_2$ TFTs by PLL treatment, the stability issue after treatment was investigated. As frequently reported in the literature, oxygen and water molecules in air could be adsorbed on the $MoTe_2$ layers, causing the instability of the electrical properties [97-99]. Moreover, the sustainability of doping effect has been reported to be unstable in air [100]. These doping effects gradually disappear and return to its initially undoped states of the $MoTe_2$ TFTs during long-term operation in air. Thus, to preserve the electrical properties without variation and degradation after doping is highly necessary. In this respect, a hydrophobic polymer, cyclic transparent optical polymer (CYTOP), was passivated on the PLL treated $MoTe_2$ TFTs because CYTOP has been known to be an effective passivation layer to improve the stability of TMDC TFTs [97, 98, 101, 102]. As a result, the CYTOP prohibits $MoTe_2$ layers with charge enhancer from reacting with ambient external gas in air, leading to freezing of V_{th} and improvement of the device stability in Fig. 4.9.

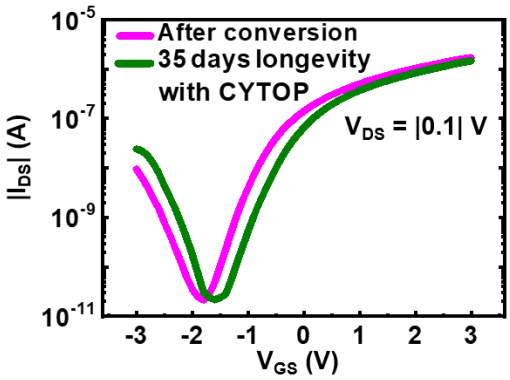

Figure 4.9 Longevity test of type-converted $MoTe_2$ TFTs after CYTOP passivation.

For the better understanding on the observed doping effects by PLL treatment, analysis of chemical/physical properties for $MoTe_2$ TFTs was examined. X-ray photoelectron spectroscopy (XPS) measurement was performed to investigate changes in the electronic structure of $MoTe_2$ induced by PLL treatment, together with their charge transfer phenomena. Figure 4.8(a) exhibits the binding energy variations for $MoTe_2$, before and after treatment with PLL, from which Mo 3d and Te 3d peaks are observed for the bare and PLL treated $MoTe_2$. After chemical doping by PLL treatment, binding energies of the Mo 3d and Te 3d peaks for $MoTe_2$ were upshifted by ~ 0.5 eV, indicating that the Fermi energy moved upwards to the conduction band edge (CBE). These results are consistent with the previously reported literature for molecular doping of TMDCs [103-108]. Then, Raman spectroscopy was employed to confirm doping effects on $MoTe_2$ TFTs, as reported elsewhere as powerful tool [102-109]. Figure 4.8(b) plots the Raman spectra of $MoTe_2$ before and after the PLL treatment. Two characteristic vibrational modes (E^1_{2g} and A^1_g) are observed near 233 and 173 cm^{-1} in the $MoTe_2$ flakes, where the E^1_{2g} mode is attributed to the in-plane

vibration between Mo and Te atoms, whereas the A^1g mode is due to the out-of-plane vibration between Mo and Te atoms. After the PLL treatment, the A^1_g and E^1_{2g} peaks were redshifted by 1.2 cm^{-1} and 0.3 cm^{-1} for $MoTe_2$ TFTs. The observed redshift of the two characteristic modes in the $MoTe_2$ TFTs describes that the n-doping effects of the PLL treatment stem from an increase in electron–phonon scattering due to the enhanced electron concentration.

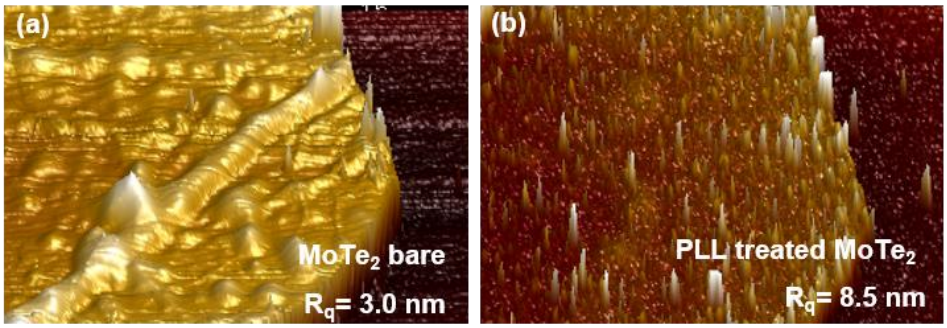

Figure 4.10 AFM topology images of $MoTe_2$ flakes (a) before and (b) after PLL treatment.

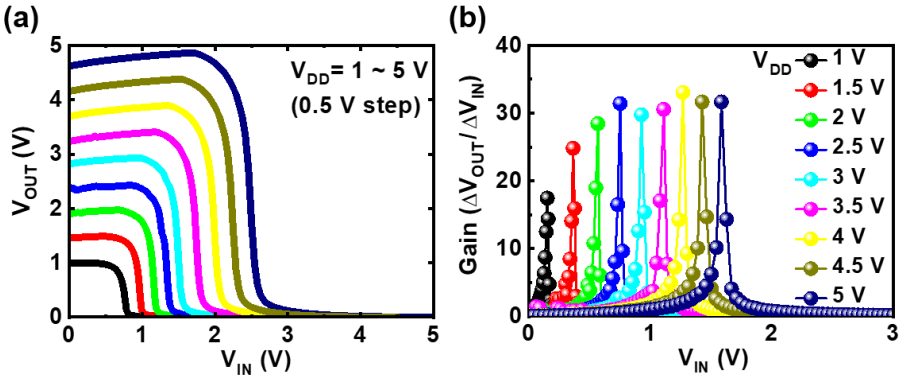

Figure 4.11 (a) Voltage transfer characteristics and (b) gain of complementary inverter composed of p-type and n-type $MoTe_2$ TFTs at various V_{DD}.

Then, AFM measurement was used to see the physical difference of $MoTe_2$ TFTs before and after PLL treatment, which revealed bumpy surface of $MoTe_2$ TFTs after PLL treatment in Fig. 4.10. This is one of evidence showing that PLL was physically covered on the $MoTe_2$ flake, leading to the change in the surface morphology [110]. The XPS, Raman, and AFM results evidently support the n-doping effects on $MoTe_2$ TFTs by PLL treatment. In addition, with the secured p-type and n-type $MoTe_2$ TFTs, complementary inverter was implemented to substantiate electrical performances of both n and p-type TFTs in the circuits. Figure 4.11 displays voltage transfer characteristics composed of p-type and n-type $MoTe_2$ TFTs, which clearly show full-swing characteristics of inverter even under low operating voltage and decent gain values.

4.4 Light-Insensitive Behaviors on Photocurrent Generation in $MoTe_2$ TFTs

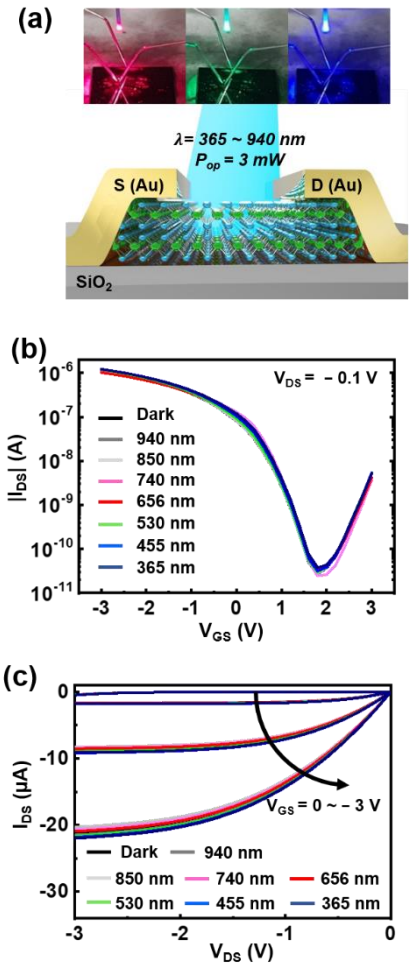

Figure 4.12 (a) A device structure of $MoTe_2$ TFT under illumination with various wavelength from 940 nm to 365 nm. (b) Transfer characteristics and (c) output characteristics of p-type $MoTe_2$ TFTs under illumination.

In the commercial display system, one of inevitable issues is photo-leakage currents generated from backplane transistors, which may render driving currents

unstable, leading to pixel variation of QLEDs. Hence, it requires a black matrix layer to block the penetration of light into the transistor and an optical feedback system to adjust the current value. In this sense, to investigate the generation of photo-leakage currents in $MoTe_2$ TFTs, photoresponse was measured under illumination with wavelength from 940 nm (NIR) to 365 nm (UV), as shown in Fig. 4.12(a). Figure 4.12(b), (c) show transfer and output characteristics of $MoTe_2$ TFTs under illumination. Interestingly, negligible generation of photocurrents under illumination of broad spectrum (NIR ~ UV) was observed at all V_{GS} and V_{DS} regions as shown in Fig. 4.12(b), (c).

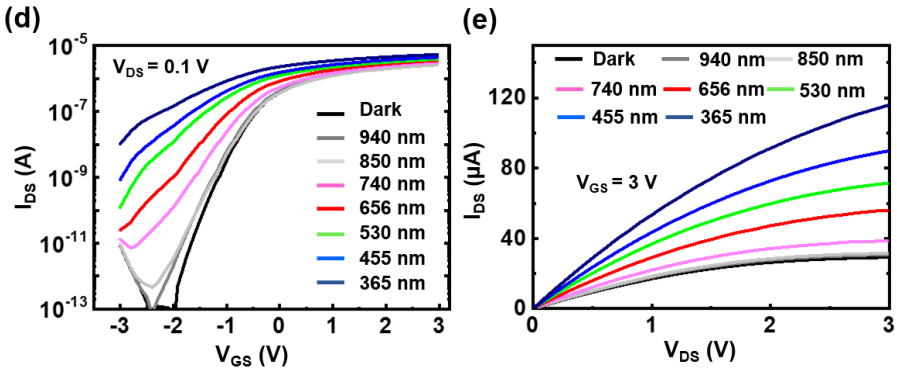

Figure 4.13 (a) Transfer characteristics and (b) output characteristics of MoS_2 TFTs under illumination.

To compare the generation of photocurrent with one of representative TMDC materials as MoS_2 for display backplane TFTs, photoresponse of MoS_2 TFTs was also measured by the same light source. As shown in Figure 4.13(a), (b), photocurrent of MoS_2 TFTs gradually increases under light exposure of shorter wavelength [107]. Moreover, Figure 4.13(e) exhibits that output current under illumination (with ~ 365 nm) is 4 times larger than that under dark condition. Detailed current levels of the

TFTs in the operation regime of on (or off) state were directly compared in Fig. 4.14, where current levels were extracted from transfer characteristics to clearly see the current variation in the off regime. MoS_2 TFTs exhibit increased currents under illumination, showing 4 times and 4 orders higher in on- and off-regimes, respectively. On the contrary, as apparently observed in Figure 4.13(b), (c), currents of $MoTe_2$ TFTs did not change under broad spectrum of light. To confirm the reproducibility of photo-immune properties of $MoTe_2$ TFTs, different $MoTe_2$ TFTs with (i) type conversion, (ii) CYTOP passivation, and (iii) another S/D metal (e.g., Al) were utilized (Figure 4.15).

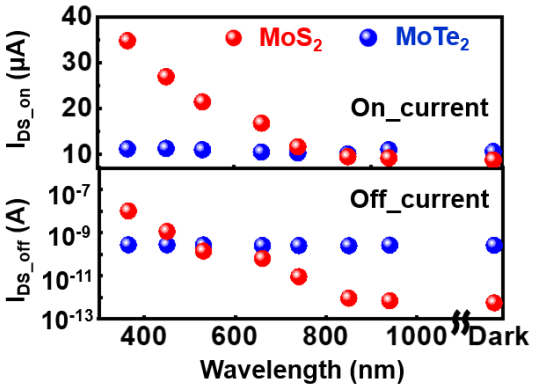

Figure 4.14 Evolution of maximum on-current and minimum off-current for $MoTe_2$ (blue circle) and MoS_2 TFTs (red circle) under illumination with various wavelength.

In this configuration, the behavior of photoresponse is similarly observed, which implies that photo-immunity is not related with the external issues such as ambient gases, contact electrodes, and type of channel, and others, but associated with intrinsic channel material property itself. In addition, there are other reports to similarly show the negligible photocurrents of multilayered $MoTe_2$ TFTs [111]. Overall, the exact

mechanism for the photo-immunity of $MoTe_2$ TFTs is not clear yet, but the light-insensitive photo-leakage current is possibly due to defects states where those are located in $MoTe_2$ layers or/and their interfaces between $MoTe_2$ layers, leading to limited generation of free-carriers even after light excitation [111]. Thus, the systematic investigation is highly required in an independent work, however, the obtained results suggest that $MoTe_2$ TFTs can have strong advantages as display backplane TFTs compared to other TMDCs and conventional materials. The photo-insensitive properties for $MoTe_2$ TFTs could be one of indispensable properties to realize the future electronic application which is highly necessary for the high security and valley electronics [112, 113].

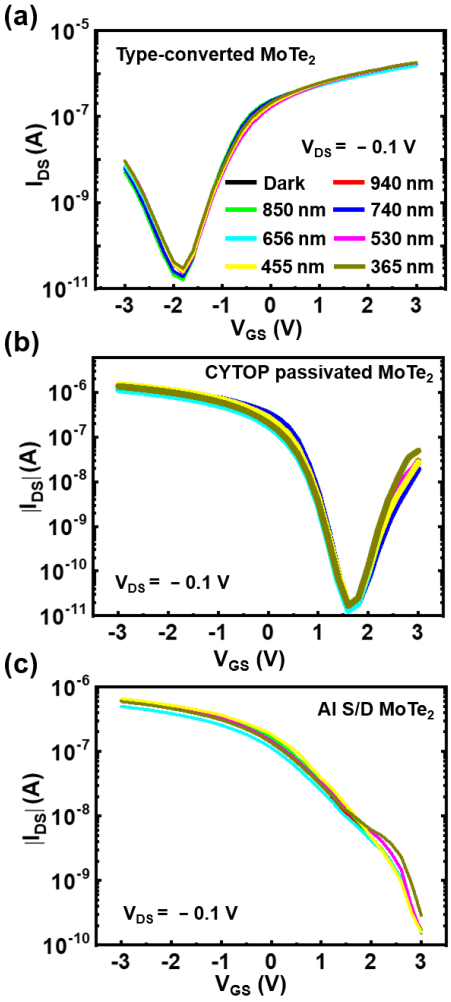

Figure 4.15 Photoresponses of (a) type-converted $MoTe_2$ TFTs, (b) CYTOP passivated $MoTe_2$ TFTs, and (c) $MoTe_2$ TFTs with S/D of aluminum in transfer characteristics at $V_{DS} = -0.1$ V.

4.5 Operation of QLEDs Driven by Channel-type Controlled $MoTe_2$ TFTs

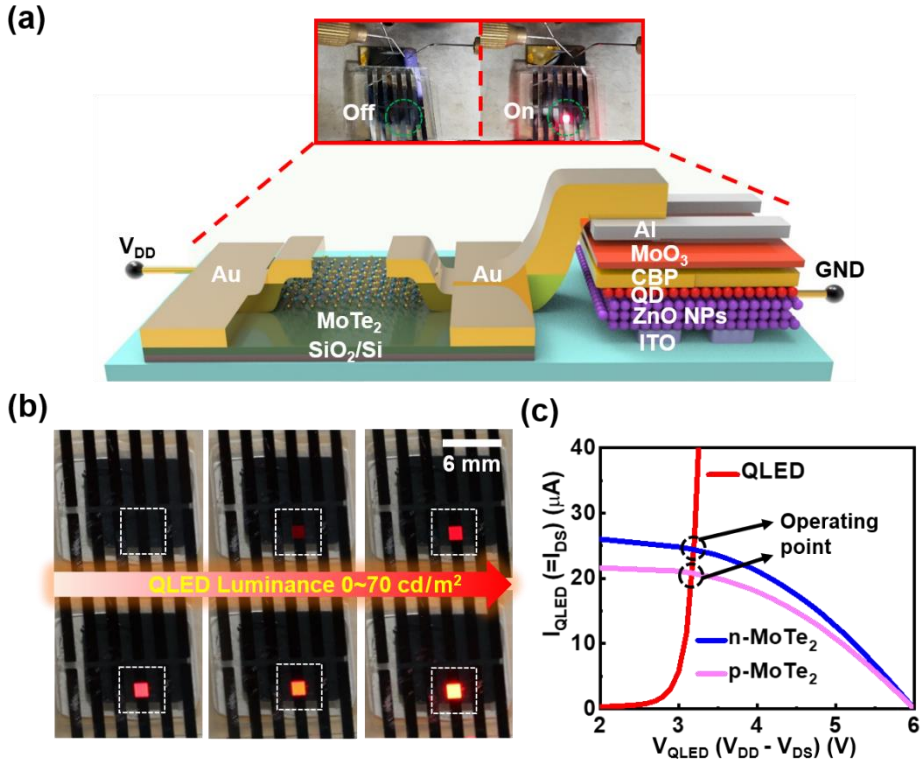

Figure 4.16 (a) An illustration of device structure for QLED operation driven by $MoTe_2$ TFT and photographs showing actual QLED operation. (b) Photographs showing brightness of QLED driven by $MoTe_2$ TFTs during V_{GS} sweeps. (c) Overlapped output curves for load-line analysis of QELD operation driven by n- and p-type $MoTe_2$ TFTs.

For validation on practical impacts for actively controlled QLEDs via channel-type controlled $MoTe_2$ TFTs, the driving capability of $MoTe_2$ TFTs for the QLEDs operation was demonstrated in Figure 4.16. Figure 4.16(a) illustrates a schematic of

device structures composed of $MoTe_2$ TFTs and QLEDs. Inset photographs denote the real operation at both on- and off-states, wherein the electrode of $MoTe_2$ TFTs is electrically connected with the anode of QLEDs by external wiring. Since the current path in the circuit is one-way, QLEDs can emit the light only when $MoTe_2$ TFTs are switched on, implying that QLEDs can be controllably driven by $MoTe_2$ TFTs. Furthermore, to efficiently operate the QLEDs, driving transistors should have a good off-current performance and provide a sufficient on-current level to the QLEDs. Based on decent electrical performance of fabricated $MoTe_2$ TFTs, the successful on-off switching of QLEDs is demonstrated as shown in Figure 4.16(a) (top). Figure 4.16(b) displays gradual changes of QLED luminance by modulating the driving current of n-type $MoTe_2$ TFTs with V_{GS} sweeping and fixed V_{DD}. As the gate voltage of $MoTe_2$ TFTs increases, drain currents of $MoTe_2$ TFTs are gradually enhanced, leading to increased brightness of QLEDs with luminance from 0 to 70 cd/m^2. Additionally, we also confirmed operation of QLEDs driven by p-type $MoTe_2$ and n-type $MoTe_2$ TFTs with the same channel material (e.g., multilayered $MoTe_2$). With the respect to pixel configuration connected with driving transistors, top (or bottom) emission mode can be preferably determined by selection of either n-type channel or p-type channel. For example, when p-type driving transistors are adopted for active-matrixed pixel configuration, bottom emission on QLEDs can provide more reliable light-emitting device configuration type due to easy adoption of thicker top-electrodes, leading to reliable passivation on the layers of QLED pixel. However, for monolithic integration with complimentary driving circuits in active-matrix pixel configuration, both of n and p-type transistors should be required. For this case, n-type driving transistors would be appealing due to favorable stacking configuration associated with limited doping techniques. In addition, when it comes to type converted device after n-type doping, most of n-type devices are unstable, as compared with p-type device

configuration. Thus, the process sequence requires n-type device implementation first, followed by p-type configuration. In this sense, Figure 4.16(c) demonstrates the capability on control of driving currents and symmetry on operation points in the load-line analysis when n (or p)-type driving transistor controlled the currents in the QLED pixel. Figure 4.16(c) plots overlapped output characteristics of QLEDs and $MoTe_2$ TFTs, wherein intersection points were marked as circles to indicate operating points driven by each TFT. This is because the supply voltage (V_{DD}) is divided into QLEDs and $MoTe_2$ TFTs considering relative resistances so that current values of QLEDs and $MoTe_2$ TFTs are supposed to be same in the circuit. Overall, the behaviors of QLEDs by p-type $MoTe_2$ TFTs are similar with those by n-type $MoTe_2$ TFTs. This is a good sign of easiness to select of driving transistors which are connected with the pixels due to symmetry on current drivability for n (or p)-type driving transistors.

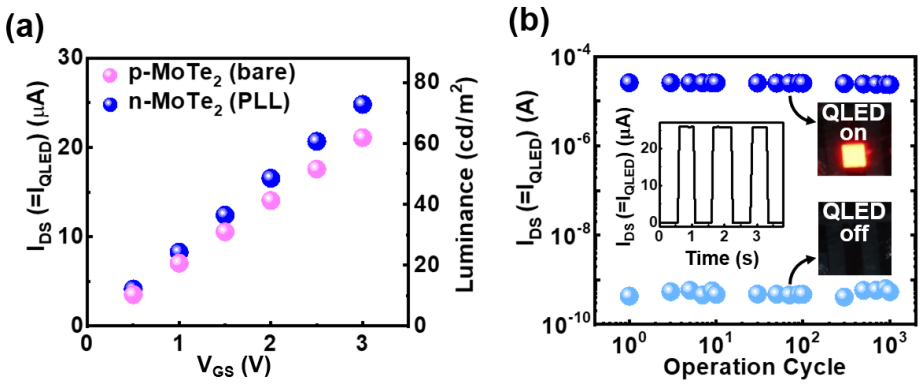

Figure 4.17 (a) Evolution of driving currents of n- and p-type $MoTe_2$ TFTs at various V_{GS}, which indicates the control of currents and luminance via PLL treatment. (b) Stability test of QLED operation driven by n-type $MoTe_2$ TFTs during measurement of 1000 cycles. Inset figure plots switching properties of driving currents under pulsed V_{GS}.

In addition, apparent display on QLED current can be nicely controlled by n (or p)-type driving transistors in Fig. 4.17(a). Even after the type conversion of p-type $MoTe_2$ TFTs by PLL treatment, the luminance according to operation currents which are determined by load-line analysis was well matched regardless of n (or p)-type of channel for $MoTe_2$ TFTs. This demonstration validates the entire the device stability before and after type conversion of driving transistors. Moreover, the operation stability issues are investigated. Figure 4.17(b) shows a multicycle measurement of QLED operation driven by $MoTe_2$ TFTs at a fixed bias condition of V_{DD} (=6 V) and pulsed V_{GS} (3 V, t_d = 1 s). As a result, it elucidated the negligible variation of driving currents at on- and off-current regimes and stable operation by 10^3 cycles. Furthermore, the inset figure reveals a behavior of dynamic operation at pulsed V_{GS}, from which clear switching properties and response from input signal without noticeable delay time were obtained. The demonstration finally validates that operating points for pixel currents in QLEDs and driving transistors are highly sustainable, displaying that driving $MoTe_2$ TFTs are highly reliable even after multiple cycles under illumination of QLEDs during on-state regime. This is attributed to the light-insensitive behaviors on driving transistors of $MoTe_2$ TFTs during light illumination. Consequently, all the results were successfully demonstrated, showing the driving capability of $MoTe_2$ TFTs as next-generation display backplane transistors of QLEDs.

4.6 Summary

In conclusion, we firstly demonstrated the operation of surface ligand modified QLEDs display driven by $MoTe_2$ TFTs with achievement of the systematic and reliable type conversion. For the high performance and stable operation of the whole display system, we adopted the molecular doping strategy using PLL treatment to convert initial p-type characteristics to n-type characteristics of $MoTe_2$ backplane TFTs. The evidence of n-type doping effect was elucidated by XPS, Raman spectroscopy, AFM, and electrical characteristics. Furthermore, decent electrical properties of $MoTe_2$ TFTs were obtained such as the SS, V_{th}, field effect mobility, hysteresis gap, and on-off ratio before/after n-type doping. Also, inverted bottom emissive QLEDs exhibited high current efficiency and long-term operational lifetimes via ligand modification. The presence of ligand modification was investigated by FTIR, UPS, and UV-Visible absorption. As a result, the driving capability of light-insensitive $MoTe_2$ TFTs for the operation of QLEDs display provides the successful and advanced applications as next-generation display backplane transistors of QLEDs. With the preferable control of channel type of $MoTe_2$ TFTs and its light-insensitive photocurrent behaviors for n (or p)-type $MoTe_2$ TFTs, active-matrixed QLEDs are potentially applicable to the envision applications; (i) highly stacked monolithic, invisible QLED displays with high robustness over bending and stretchable environments, (ii) bio-implantable devices with bio-imaging capability which enables to induce light-excitation and its detection in the implanted device environment, and (iii) light-to-frequency conversion circuits which require high standard of noise immunity and its data security, and others.

Chapter 5

Conclusion

In this thesis, we discussed oxide/nano material based thin film transistor as a backplane and quantum dot light-emitting diode as a display for future applications.

Firstly, we demonstrated p-type SnO TFTs with spray-coated SWNTs as an alternative source and drain electrodes comparable to conventional metal. For the wearable device configuration, we analyzed electrical contact properties and their reliabilities were systematically extracted by using gated TLM method. Also, adoption of PMMA as an encapsulation layer effectively improved device contact. In addition, field effect mobility and activation energy indicate that all the properties are preserved during these processes. As a result, SWNTs as an alternative electrode are practical options among various candidates for the wearable devices.

Secondly, QLEDs display driven by $MoTe_2$ TFTs was firstly demonstrated. For high brightness and reliable operation, we adopted the molecular doping system in

TMDCs TFFs and ligand modification method in QLEDs, respectively. First, our molecular doping methodology via PLL treatment could convert initial p-type characteristics to n-type characteristics of $MoTe_2$. Also, doping characteristics were systematically analyzed by XPS, Raman spectroscopy, AFM, and their electrical properties. Second, for the high current efficiency and long-term operation of QLEDs, we modified ligands of QDs to enhance the conductivity of QDs and control the VBM without changing bandgap. Based on these methods, we showed the driving capabilities of QLEDs based on both n and p type $MoTe_2$ TFTs.

In this thesis, we not only provide systematical analysis of p-type oxide/nano materials-based semiconductor to confirm its availability as backplane TFTs but also demonstrate the operation of QLEDs with type controllable TMDC TFTs. For low power consumption and highly bright display, type controllable and light-insensitive TFTs are indispensable to minimize the pixel variation. As a result, adoption of p-type oxide/nano materials and type-controllable methodology of TMDC TFTs could be one of viable options to meet optimized device configuration, which is well-matched with the process of QLEDs such as normal/inverted architecture.

Bibliography

[1] P. Weimer, "The TFT, a new thin-film transistor", *Proc. IRE,* ***50****,* 6 (1962)

[2] H. J. Jang, J. Y. Lee, J. Kwak, D. Lee, J.-H. Park, B. Lee and Y. Y. Noh, "Progress of display performance: AR, VR, QLED, OLED, and TFT", *J. Inf. Disp,.* ***20****,* 1 (2019).

[3] K. Nomura, H. Ohta, A. Takagi, T. Kamiya, M. Hirano, and H. Hosono, "Room-temperature fabrication of transparent flexible Thin-Film Transistors using amorphous Oxide semiconductors," *Nature,* ***432****,* 7016 (2004).

[4] E. Fortunato, P. Barquinha, and R. Martins, "Oxide Semiconductor Thin-Film Transistors: A Review of Recent Advances," Advanced Material, 24, 22, (2012).

[5] J. S. Park, W.-J. Maeng, H.-S. Kim, and J.-S. Park, Review of recent developments in amorphous oxide semiconductor thin-film transistor devices, Thin Solid Film, 520, 6 (2012)

[6] A. Togo, F. Oba, and I. Tanak, "First-principles caculations of native defects in tin monoxide", Phys, Rev. B, 74, 195128 (2006).

[7] B. Radosavljevic, A. Radenovic, J. Brivio, V. Giacometti, and A. Kis, "Single-layer MoS_2 transistor", *Nat. Nanotechnol.,* ***6****,* 3 (2011)

[8] S. Bertolazzi, J. Brivio, A. Kis, "Stretching and Breaking of Ultrathin MoS_2", *ACS Nano,* ***5****,* 12 (2011)

[9] K. F. Mak, C. Lee, J. Hone, J. Shan, and T. F. Heinz, "Atomically Thin MoS_2: A New Direct-Gap Semiconductor", *Phys. Rev.Lett.,* ***105****,* 13 (2010)

[10] S. Chuang, R. Kapadia, H. Fang, T. Chia Chang, W.-C. Yen, Y.-L. Chueh, A. Javey, "Near-Ideal Electrical Properties of InAs/WSe_2 Van Der Waals Heterojunction Diodes", *Appl. Phys. Lett.,* ***102****,* 242101 (2013)

[11] P. Tonndorf, R. Schmidt, P. Bottger, X. Zhang, J. Borner, A. Liebig, M. Albrecht, C. Kloc, O. Gordan, D. R. T. Zahn, S. M. D. Vasconcellos, and R. Bratschitsch,

"Photoluminescence Emission and Raman Response of Monolayer MoS_2, $MoSe_2$, and WSe_2", *Opt. Express*, ***21***, 4 (2013).
[12] M. Choi, Y. J. Park, B. K. Sharma, S.-R. Bae, S. Y. Kim, J.-H. Ahn, "Flexible active-matrix organic light-emitting diode display enabled by MoS_2 thin-film transistor, *Sci. Adv.*, ***4***, 4 (2018)
[13] M. Tosun, L. Chan, M. Amani, T. Roy, G. H. Ahn, P. Taheri, C. Carraro, J. W. Ager, R. Maboudian, and A. Javey, "Air-stable n-Doping of WSe_2 by Anion Vacancy Formation with Mild Plasma Treatment, *Acs Nano*, ***10***, 7 (2016).
[14] S.-H. Jo, D.-H. Kang, J. Shim, J. Jeon, M. H. Jeon, G. Yoo, J. Kim, J. Lee, G. Y. Yeom, S. Lee, H.-Y. Yu, C. Choi, and J.-H. Park, "A High-Performance WSe_2/h-BN Photodetector using aTriphenylphophine (PPh_3)-Based n-Doping Technique, *Adv. Mater.*, ***28***, 24 (2016)
[15] D. Kiriya, M. Tosun, P. D. Zhao, J. S. Kang, A. Javey, "Air-stable surface charge transfer doping of MoS_2 by benzyl viologen", *J. Am. Chem. Soc.*, ***136***, 22 (2014).
[16] L. M. Yang, K. Majumdar, H. Liu, Y. C. Du, H. Wu, M. Hatzistergos, P. Y. Hung, R. Tieckelmann, W. Tsai, C. Hobbs, P. D. Ye, "Chloride molecular doping technique on 2D materials: WS_2 and MoS_2" *Nano Lett.*, ***14***, 12 (2014).
[17] Y. J. Park, A. K. Katiyar, A. T. Hoang, and J.-H. Ahn, "Controllable P- and N-Type Conversion of $MoTe_2$ via Oxide Interfacial Layer for Logic Circuits", *Small*, ***15***, 28 (2019)
[18] V. I. Klimov, Nanocrystal quantum dots, *CRC Press*, (2017).
[19] Y. Shirasaki, G. J. Supran, M. G. Bawendi, and V. Bulović,"Emergence of colloidal quantum-dot light-emitting technologies" *Nat. Photonics*, ***7***, 1 (2013)
[20] J. Lim, Y. S. Park, and V. I. Klimov,"Optical gain in colloidal quantum dots achieved with direct-current electrical pumping" *Nat. Mater.*, ***17***, 1 (2018)
[21] O. V. Kozlov, Y. S. Park, J. Roh, I. Fedin, T. Nakotte, and V. I. Klimov,"Sub-single-exciton lasing using charged quantum dots coupled to a distributed feedback cavity" *Science*, ***365***, 6454 (2019)
[22] V. I. Klimov, S. A. Ivanov, J. Nanda, M. Achermann, I. Bezel, J. A. McGuire, and A. Piryatinski,"Single-exciton optical gain in semiconductor nanocrystals" *Nature*, ***447***, 7143 (2007)
[23] K. F. Wu, Y. S. Park, J. Lim, and V. I. Klimov,"Towards zero-threshold optical gain using charged semiconductor quantum dots" *Nat. Nanotechnol.*, ***12***, 12 (2017)
[24] E. H. Sargent,"Colloidal quantum dot solar cells" Nature Photonics, 6, 3 (2012)
[25] C.-H. M. Chuang, P. R. Brown, V. Bulović, and M. G. Bawendi,"Improved performance and stability in quantum dot solar cells through band alignment engineering" *Nat. Mater.*, ***13***, 8 (2014)
[26] J. K. Jaiswal, E. R. Goldman, H. Mattoussi, and S. M. Simon,"Use of quantum dots for live cell imaging" *Nat. methods*, ***1***, 1 (2004)
[27] V. L. Colvin, M. C. Schlamp, and A. P. Alivisatos," Light-emitting diodes made from cadmium selenide nanocrystals and a semiconducting polymer" *Nature*, ***370***, 6488 (1994).
[28] L. Brus,"Electronic wave functions in semiconductor clusters: experiment and theory" *J. Phys. Chem.*, ***90***, 12 (1986).

[29] X. Peng, M. C. Schlamp, A. V. Kadavanich, and A. P. Alivisatos, " Epitaxial Growth of Highly Luminescent CdSe/CdS Core/Shell Nanocrystals with Photostability and Electronic Accessibility", *J. Am. Chem. Soc.*, ***119***, 30 (1997).
[30] D. V. Talapin and J. Steckel, "Quantum dot light-emitting devices", *MRS Bulletin*, ***38***, 9 (2013)
[31] W. K. Bae, S. Brovelli, and V. I. Klimov,"Spectroscopic insights into the performance of quantum dot light-emitting diodes" *MRS bulletin*, ***38***, 9 (2013).
[32] J. Kwak, W. K. Bae, D. Lee, I. Park, J. Lim, M. Park, H. Cho, H. Woo, D. Y. Yoon, K. Char, S. Lee, and C. Lee, "Bright and efficient full-color colloidal quantum dot light-emitting diodes using an inverted device structure", *Nano Lett.*, ***12***, 5 (2012).
[33] X. Dai, Z. Zhang, Y. Jin, Y. Niu, H. Cao, X. Liang, L. Chen, J. Wang, and X. Peng, "Solution-processed, high-performance light-emitting diodes based on quantum dots" *Nature*, ***515***, 7525 (2014).
[34] W. Cao, C. Xiang, Y. Yang, Q. Chen, L. Chen, X. Yan, and L. Qian, "Highly stable QLEDs with improved hole injection via quantum dot structure tailoring" *Nat. Commun.* ***9***, 2608 (2018).
[35] Q. Su, Y. Sun, H. Zhang, and S. Chen, "Origin of Positive Aging in Quantum-Dot Light-Emitting Diodes", *Adv. Sci.*, ***5***, 10 (2018).
[36] H. Moon, and H. Chae, "Efficiency Enhancement of All-Solution-Processed Inverted-Structure Green Quantum Dot Light-Emitting Diodes Via Partial Ligand Exchange with Thiophenol Derivatives Having Negative Dipole Moment" *Adv. Optical Mater.*, ***8***, 1 (2020).
[37] J. Song, O. Wang, H. Shen, Q. Lin, Z. Li, L. Wang, X. Zhang, and L. S. Li, "Over 30% External Quantum Efficiency Light-Emitting Diodes by Engineering Quantum Dot-Assisted Energy Level Match for Hole Transport Layer" *Adv. Funct. Mater.*, ***29***, 33 (2019).
[38] J. R. Manders, L. Qian, A. Titov, J. Hyvonen, J. T. Scott, K. P. Acharya, Y. Yang, W. Cao, Y. Zheng, J. Xue, and P, H. Holloway, "High efficiency and ultra-wide color gamut quantum dot LEDs for next generation displays", *J. Soc. Inf. Disp.*, ***23***, 7 (2015).
[39] Z. Li, Y. Hu, H. Shen, Q. Lin, L. Wang, H. Wang, W. Zhao, and L. S. Li, "Efficient and long-life green light-emitting diodes comprising tridentate thiol capped quantum dots", *Laser Photon. Rev.*, ***11***, 1600227 (2017).
[40] X. Li, Y. B. Zhao, F. Fan, L. Levina, M. Liu, R. Q. Bermudez, X. Gong, L. N. Quan, J. Z. Fan, Z. Yang, S. Hoogland, O. Voznyy, Z. H. Lu, and E. H. Sargent, "Bright colloidal quantum dot light-emitting diodes enabled by efficient chlorination", *Nat. Photonics*, ***12***, 159 (2018).
[41] Z. Yang, Q. Wu, G. Lin, X. Zhou, W. Wu, X. Yang, J. Zhang, and W. Li, "All-solution processed inverted green quantum dot light-emitting diodes with concurrent high efficiency and long lifetime", *Mater. Horiz.*, ***6***, 10 (2019).
[42] Y. Sun, Q. Su, H. Zhang, F. Wang, S. Zhang, and S. Chen, "Investigation on Thermally Induced Efficiency Roll-Off: Toward Efficient and Ultrabright Quantum-Dot Light-Emitting Diodes", *ACS nano*, ***13***, 10 (2019).

[43] H. Shen, W. Cao, N. T. Shewmon, C. Yang, L. S. Li, and J. Xue, "High-efficiency, low turn-on voltage blue-violet quantum-dot-based light-emitting diodes", *Nano Lett.*, ***15***, 2 (2015).
[44] L. Wang, J. Lin, Y. Hu, X. Guo, Y. Lv, Z. Tang, J. Zhao, Y. Fan, N. Zhang, Y. Wang, and X. Liu, "Blue Quantum Dot Light-Emitting Diodes with High Electroluminescent Efficiency", *ACS Appl. Mater. Interfaces*, ***9***, 44 (2017).
[45] Q. Lin, L. Wang, Z. Li, H. Shen, L. Guo, Y. Kuang, H. Wang, and L. S. Li, "Nonblinking Quantum-Dot-Based Blue Light-Emitting Diodes with High Efficiency and a Balanced Charge-Injection Process", *ACS Photonics*, ***5***, 3 (2018).
[46] D. Li, J. Bai, T. Zhang, C. Chang, X. Jin, Z. Huang, B. Xu, and Q. Li, "Blue quantum dot light-emitting diodes with high luminance by improving the charge transfer balance", *Chem. Commun.*, ***55***, 24 (2019).
[47] S. Rhee, J. H. Chang, D. Hahm, B. G. Guk, J. Kim, H. Lee, J. Lim, E. Hwang, J. Kwak, and W. K. Bae, Tailoring the Electronic Landscape of Quantum Dot Light-Emitting Diodes for High Brightness and Stable Operation, *Acs Nano*, ***14***, 12 (2020)
[48] Y. Liu, H. Zhou, R. Cheng, W. Yu, Y. Huang, and X. Duan, "Highly Flexible Electronics from Scalable Vertical Thin Film transistors," *Nano Lett.*, ***14***, 3 (2014).
[49] Y.-. Li, J.-C. He, S.-M. Hsu, C.-C. Lee, D.-Y. Su, F.-Y. Tsai, and I-C. Cheng, "Flexible Complementary Oxide–Semiconductor-Based Circuits Employing n-Channel ZnO and p-Channel SnO Thin-Film Transistors," *IEEE Electron Device Lett.*, ***37***, 1, (2015)
[50] S. H. Jin, S.-K. Kang, I.-T. Cho, S. Y. Han, H. U. Chung, D. J. Lee, J. Shin, G. W. Baek, T.-i. Kim, J.-H. Lee, and J. A. Rogers, "Water-Soluble Thin Film Transistors and Circuits Based on Amorphous Indium–Gallium–Zinc Oxide," *ACS Appl. Mater. Interfaces*, ***7***, 15 (2015).
[51] E. B. Secor, J. Smith, T. J. Marks, and M. C. Hersam, "High-Performance Inkjet-Printed Indium-Gallium-Zinc-Oxide Transistors Enabled by Embedded, Chemically Stable Graphene Electrodes," *ACS Appl. Mater. Interfaces*, ***8***, 27 (2016)
[52] E. Fortunato, R. Barros, P. Barquinha, V. Figueiredo, S.-H. K. Park, C.-S. Hwang, and R. Martins, "Transparent p-type SnO_x thin film transistors produced by reactive RF magnetron sputtering followed by low temperature annealing," *Appl. Phys. Lett.*, ***97***, 5 (2010).
[53] S. Y. Kim, C. H. Ahn, J. H. Lee, Y. H. Kwon, S. Hwang, J. Y. Lee, and H. K. Cho, "p-Channel Oxide Thin Film Transistors Using Solution-Processed Copper Oxide," *ACS Appl. Mater. Interfaces*, ***5***, 7 (2013).
[54] A. Liu, G. Liu, H. Zhu, B. Shin, E. Fortunato, R. Martins, and F. Shan, "Hole mobility modulation of solution-processed nickel oxide thin-film transistor based on high-k dielectric", *Appl. Phys. Lett.* ***108***, 23 (2016)
[55] S. H. Jin, J. Shin, I.-T. Cho, S. Y. Han, D. J. Lee, C. H. Lee, J.-H. Lee, and J. A. Rogers, "Solution-Processed Single-Walled Carbon Nanotube Field Effect Transistors and Bootstrapped Inverters for Disintegratable, Transient Electronics," *Appl. Phys. Lett.*, ***105***, 1 (2014).

[56] C.-H. Yu, H.-C. Wu, and C.-H. Chien, “Effect of passivation layer on InGaZnO thin-film transistors with hybrid silver nanowires as source and drain electrodes,” *Jpn. J. Appl. Phys.*, ***54***, 8 (2015).
[57] G. Chen, R. C. Davis, D. N. Futaba, S. Sakurai, K. Kobashi, M. Yumura, K. Hata, “A sweet spot for highly efficient growth of vertically aligned single-walled carbon nanotube forests enabling their unique structures and properties”, *Nanoscale*, ***8***, 1 (2016).
[58] H.-J. Kim, C.-Y. Jeong, S.-D. Bae, J.-H. Lee, and H.-I. Kwon, “Charge Transport Mechanism in p-Channel Tin Monoxide Thin-Film Transistors,” *IEEE Electron Device Lett.*, ***38***, 4 (2017).
[59] W. Kim, A. Javey, O. Vermesh, Q. Wang, Y. Li, and H. Dai, “Hysteresis Caused by Water Molecules in Carbon Nanotube Field-Effect Transistors,” *Nano Lett.*, ***3***, . 2 (2003).
[60] J. Zaumseil, K. W. Baldwin, and J. A. Rogers, “Contact resistance in organic transistors that use source and drain electrodes formed by soft contact lamination,” *J. Appl. Phys.*, ***93***, 10 (2003).
[61] G. J. Hu, C. Chang, and Y.-T. Chia, “Gate-Voltage-Dependent Effective Channel Length and Series Resistance of LDD MOSFET’s,” *IEEE Electron Device Lett.*, ***34***, 12 (1987).
[62] M. Shiraishi, M. Ata, “Work function of carbon nanotubes,” *Carbon*, ***39***, 12 (2001).
[63] W. Wang, L. Li, C. Lu, Y. Liu, H. Lv, G. Xu, Z. Ji, and M. Liu" Analysis of the contact resistance in amorphous InGaZnO thin film transistors”, *Appl. Phys. Lett.*, ***107***, 6 (2015)
[64] B. L. Sharma, Metal-Semiconductor Schottky Barrier Junctions and Their Applications (Plenum, New York, 1984).
[65] P.-C. Hsu, W.-C. Chen, Y.-T. Tsai, Y.-C. Kung, C.-H. Chang, C.-J. Hsu, C.-C. Wu, and H.-H. Hsieh, “Fabrication of p-type SnO thin-film transistors by sputtering with practical metal electrodes,”Jpn. J. Appl. Phys., 52, 5S1 (2013).
[66] S. H. Jin, K. D. Jung, H. Shin, B.-G. Park, J. D. Lee, “Grain size effects on contact resistance of top-contact pentacene TFTs”, *Synthetic Met.* ***156***, 2-4 (2006).
[67] Y.-J. Han, Y.-J. Choi, I.-T. Cho, S. H. Jin, J.-H. Lee, and and H.-I. Kwon " Improvement of Long-Term Durability and Bias Stress Stability in p-Type SnO Thin-Film Transistors Using a SU-8 Passivation Layer ," *IEEE Electron Device Lett.*, ***35***, 12 (2014).
[68] Y.-J. Han, Y.-J. Choi, H. Jeong, H.-I. Kwon, “Investigation of Intrinsic Electrical Characteristics and Contact Effects in p-Type Tin Monoxide Thin-Film Transistors Using Gated-Four-Probe Measurements”, *J. Nanosci. Nanotechnol.* ***15***, 10 (2015)
[69] X. Zeng, X. Xu, P. M. Shenai, E. Kovalev, C. Baudot, N. Mathews, and Y. Zhao, “Characteristics of the Electrical Percolation in Carbon Nanotubes/Polymer Nanocomposites”, *J. Phys. Chem. C*, ***115***, 44 (2011).
[70] J. Zhang, X. Kong, J. Yang, Y. Li, J. Wilson, J. Liu, Q. Xin, Q. Wang, and A. Song, “Analysis of carrier transport and band tail states in p-type tin monoxide thin-film transistors by temperature dependent characteristics”, *Appl. Phys. Lett.*, ***108***, 26 (2016).

[71] Q. Sun, Y. A. Wang, L. S. Li, D. Wang, T. Zhu, J. Xu, C. Yang, Y. Li, "Bright, multicoloured light-emitting diodes based on quantum dots", *Nat. Photon.*, ***1***, 717 (2007).
[72] Y. Shirasaki, G. J. Supran, M. G. Bawendi, V. Bulovic´, "Emergence of colloidal quantum-dot light-emitting technologies", *Nat. Photon.*, ***7***, 13 (2013).
[73] Y.-H. Won, O. Cho, T. Kim, D.-Y. Chung, T. Kim, H. Chung, H. Jang, J. Lee, D. Kim, E. Jang, "Highly efficient and stable InP/ZnSe/ZnS quantum dot light-emitting diodes", *Nature*, ***575***, 634 (2019).
[74] W. K. Bae, J. Kwak, J. W. Park, K. Char, C. Lee, S. Lee, "Highly Efficient Green-Light-Emitting Diodes Based on CdSe@ZnS Quantum Dots with a Chemical-Composition Gradient", *Adv. Mater.*, ***21***, 1690−1694 (2009).
[75] S. Rhee, J. H. Chang, D. Hahm, K. Kim, B. G. Jeong, H. J. Lee, J. Lim, K. Char, C. Lee, and W. K. Bae, ""Positive incentive" approach to enhance the operational stability of quantum dot-based light-emitting diodes", *ACS Appl. Mater. Interfaces*, ***11***, 40252 (2019).
[76] C. Pu, X. Dai, Y. Shu, M. Zhu, Y. Deng, Y. Jin, X. Peng, "Electrochemically-stable ligands bridge the photoluminescence-electroluminescence gap of quantum dots", *Nat. Commun.*, ***11***, 937 (2020).
[77] J. F. Wager, "Flat-Panel-Display Backplanes: LTPS or IGZO for AMLCDs or AMOLED Displays?", *Inf. Disp.*, ***30***, 26 (2014).
[79] S. G. Seo, S. H. Jin, "Photosensitive Complementary Inverters Based on n-Channel MoS_2 and p-Channel $MoTe_2$ Transistors for Light-to-Frequency Conversion Circuits", *Phys. Status Solidi - Rapid Res. Lett.*, ***13***, 1900317 (2019).
[80] H. Hosono, J. Kim, Y. Toda, T. Kamiya, S. Watanabe, "Transparent amorphous oxide semiconductors for organic electronics: Application to inverted OLEDs", *Proc. Natl. Acad. Sci. U. S. A.*, ***114***, 233 (2017).
[81] A. K. Geim, I. V. Grigorieva, "Van der Waals heterostructures", *Nature*, ***499***, 419 (2013).
[82] X. Huang, Z. Zeng, H. Zhang, "Metal dichalcogenide nanosheets: preparation, properties and applications", *Chem. Soc. Rev.*, ***42***, 1934 (2013).
[83] M. Chhowalla, H. S. Shin, G. Eda, L. J. Li, K. P. Loh, H. Zhang, "The chemistry of two-dimensional layered transition metal dichalcogenide nanosheets", *Nat. Chem.*, ***5***, 263 (2013).
[84] B. Radisavljevic, A. Radenovic, J. Brivio, V. Giacometti, A. Kis, "Single-layer MoS_2 transistors", *Nat. Nanotechnol.*, ***6***, 147 (2011).
[85] T.-H. Kim, C.-S. Lee, S. Kim, J. Hur, S. Lee, K. W. Shin, Y-Z. Yoon, M. K. Choi, J. Yang, D.-H. Kim, T. Hyeon, S. Park, S. Hwang, "Fully Stretchable Optoelectronic Sensors Based on Colloidal Quantum Dots for Sensing Photoplethysmographic Signals", *Acs nano*, ***11***, 5992 (2017).
[86] Y.-F. Li, S.-Y. Chou, P. Huang, C. Xiao, X. Liu, Y. Xie, F. Zhao, Y. Huang, J. Feng, H. Zhong, H.-B. Sun, Q. Pei, "Stretchable Organometal-Halide-Perovskite Quantum-Dot Light-Emitting Diodes", *Adv. Mater.*, ***31***, 1807516 (2019).
[87] V.Yadav, S. Roy, P. Singh, Z. Khan, A. Jaiswal, "2D MoS_2-Based Nanomaterials for Therapeutic, Bioimaging, and Biosensing Applications", *Small*, ***15***, 1803706 (2019).

[88] J. Roh, J. H. Ryu, G. W. Baek, H. Jung, S. G. Seo, K. An, B. G. Jeong, D. C. Lee, B. H. Hong, W. K. Bae, J. H. Lee, C. Lee, S. H. Jin, "Threshold Voltage Control of Multilayered MoS_2 Field-Effect Transistors via Octadecyltrichlorosilane and their Applications to Active Matrixed Quantum Dot Displays Driven by Enhancement-Mode Logic Gates", *Small*, ***15***, 1803852 (2019).
[89] J. Choi, W. Lee, J. W. Namgoong, T. M. Kim, J. P. Kim, "Synthesis and characterization of novel triazatetrabenzcorrole dyes for LCD color filter and black matrix", *Dye. Pigment.*, ***99***, 357 (2013).
[90] P. Rastogi, F. Palazon, M. Prato, F. D. Stasio, R. Krahne, "Enhancing the Performance of CdSe/CdS Dot-in-Rod Light-Emitting Diodes via Surface Ligand Modification", *Acs Appl. Mater. Interfaces*, ***10***, 5665 (2018).
[91]C. Ruppert, O. B. Aslan, T. F. Heinz, "Optical Properties and Band Gap of Single- and Few-Layer $MoTe_2$ Crystals", *Nano Lett.*, ***14***, 6231 (2014).
[92] X. Jin, C. Chang, W. Zhao, S. Huang, X. Gu, Q. Zhang, F. Li, Y. Zhang, and Q. Li, "Balancing the Electron and Hole Transfer for Efficient Quantum Dot Light-Emitting Diodes by Employing a Versatile Organic Electron-Blocking Layer", *ACS Appl. Mater. Interfaces*, ***10***, 15803 (2018).
[93] Y. Lee, B. G. Jeong, H. Roh, J. Roh, J. Han, D. C. Lee, W. K. Bae, J.-Y, Kim, C. Lee, "Enhanced Lifetime and Efficiency of Red Quantum Dot Light-Emitting Diodes with Y-Doped ZnO Sol–Gel Electron-Transport Layers by Reducing Excess Electron Injection", *Adv. Quantum. Technol.*, ***1***, 1700006 (2018).
[94] R. Wang, Y. Shang, P. Kanjanaboos, W. Zhou, Z. Ning, and E. H. Sargent, "Colloidal quantum dot ligand engineering for high performance solar cells", *Energy Environ. Sci.* ***9***, 1130-1143 (2016).
[95] Y. Li, C. Xu, P. Hu, L. Zhen, "Carrier Control of MoS_2 Nanoflakes by Functional Self-Assembled Monolayers", *ACS Nano*, ***7***, 7795 (2013).
[96] D. M. Sim, M. Kim, S. Yim, M. J. Choi, J. Choi, S. Yoo, Y. S. Jung, "Controlled Doping of Vacancy-Containing Few-Layer MoS_2 via Highly Stable Thiol-Based Molecular Chemisorption", *ACS Nano*, ***9***, 12115 (2015).
[97] S. G. Seo, J. H. Hong, J. H. Ryu, S. H. Jin, "Low-Frequency Noise Characteristics in Multilayer $MoTe_2$ FETs With Hydrophobic Amorphous Fluoropolymers", *IEEE Electron Device Lett.*, ***40***, 251 (2019).
[98] G. Seo, J. Jeong, S. H. Jin, "Reversible and controllable threshold voltage modulation for n-channel MoS_2 and p-channel $MoTe_2$ field-effect transistors via multiple counter doping with ODTS/poly-L-lysine charge enhancers", *Microelectron. Reliab.*, ***111***, 113680 (2020).
[98] K. Cho, W. Park, J. Park, H. Jeong, J. Jang, T. Y. Kim, W. K. Hong, S. Hong, T. Lee, "Electric Stress-Induced Threshold Voltage Instability of Multilayer MoS_2 Field Effect Transistors", *ACS Nano*, ***7***, 7751 (2013).
[99] D. H. Kang, J. Shim, S. K. Jang, J. Jeon, M. H. Jeon, G. Y. Yeom, W. S. Jung, Y. H. Jang, S. Lee, J. H. Park, "Controllable Nondegenerate p-Type Doping of Tungsten Diselenide by Octadecyltrichlorosilane", *ACS Nano*, ***9***, 1099 (2015).
[100] J. Roh, I. T. Cho, H. Shin, G. W. Baek, B. H. Hong, J. H. Lee, S. H. Jin, C. Lee, "Fluorinated CYTOP passivation effects on the electrical reliability of multilayer MoS_2 field-effect transistors", *Nanotechnology*, ***26***, 455201(2015).

[101] S. G. Seo, J. Joeng, K. Kim, K. Kim, S. H. Jin, "Bias Stress Instability in Multilayered MoS_2 Field-Effect Transistors Under Pulse-Mode Operation", *IEEE Trans. Electron Devices*, ***67***, 1864 (2020).
[102] H. G. Ji, P. Solís-Fernández, D. Yoshimura, M. Maruyama, T. Endo, Y. Miyata, S. Okada, H. Ago, "Chemically Tuned p- and n-Type WSe_2 Monolayers with High Carrier Mobility for Advanced Electronics", *Adv. Mater.*, ***31***, 1903613 (2019).
[103] A. Tarasov, S. Zhang, M. Y. Tsai, P. M. Campbell, S. Graham, S. Barlow, S. R. Marder, E. M. Vogel, "Controlled doping of large-area trilayer MoS_2 with molecular reductants and oxidants", *Adv. Mater.*, ***27***, 1175 (2015).
[104] J. D. Lin, C. Han, F. Wang, R. Wang, D. Xiang, S. Qin, X. A. Zhang, L. Wang, H. Zhang, A. T. S. Wee, W. Chen, "Electron-Doping-Enhanced Trion Formation in Monolayer Molybdenum Disulfide Functionalized with Cesium Carbonate", *ACS Nano*, ***8***, 5323 (2014).
[105] S. H. Jo, D. H. Kang, J. Shim, J. Jeon, M. H. Jeon, G. Yoo, J. Kim, J. Lee, G. Y. Yeom, S. Lee, H. Y. Yu, C. Choi, J. H. Park, "A High-Performance WSe_2 /h-BN Photodetector using a Triphenylphosphine (PPh_3)-Based n-Doping Technique", *Adv. Mater.*, ***28***, 4824 (2016).
[106] D. H. Kang, M. H. Jeon, S. K. Jang, W. Y. Choi, K. N. Kim, J. Kim, S. Lee, G. Y. Yeom, J. H. Park, "Self-Assembled Layer (SAL)-Based Doping on Black Phosphorus (BP) Transistor and Photodetector", *ACS Photonics*, ***4***, 1822 (2017).
[107] D. H. Kang, M. S. Kim, J. Shim, J. Jeon, H. Y. Park, W. S. Jung, H. Y. Yu, C. H. Pang, S. Lee, J. H. Park, "High-Performance Transition Metal Dichalcogenide Photodetectors Enhanced by Self-Assembled Monolayer Doping", *Adv. Funct. Mater.*, ***25***, 4219 (2015).
[108] K. Cho, M. Min, T. Y. Kim, H. Jeong, J. Pak, J. K. Kim, J. Jang, S. J. Yun, Y. H. Lee, W. K. Hong, T. Lee, "Electrical and Optical Characterization of MoS_2 with Sulfur Vacancy Passivation by Treatment with Alkanethiol Molecules", ACS Nano, 9, 8044 (2015).
[109] B. Lee, Y. Chen, F. Duerr, D. Mastrogiovanni, E. Garfunkel, E. Y. Andrei, V. Podzorov, "Modification of Electronic Properties of Graphene with Self-Assembled Monolayers", *Nano Lett.*, ***10***, 2427 (2010).
[110] M. K. Ghimire, H. Ji, H. Z. Gul, H. Yi, J. Jiang, S. C. Lim, "Defect-Affected Photocurrent in $MoTe_2$ FETs", *ACS Appl. Mater. Interfaces*, ***11***, 10068 (2019).
[111] K. F. Mak, K. He, J. Shan, T. F. Heinz, "Control of valley polarization in monolayer MoS_2 by optical helicity", *Nat. Nanotechnol.*, ***7***, 494 (2012).
[112] T. Cao, G. Wang, W. Han, H. Ye, C. Zhu, J. Shi, Q. Niu, P. Tan, E. Wang, B. Liu, J. Feng, "Valley-selective circular dichroism of monolayer molybdenum disulphide", *Nat. Commun.*, ***3***, 887 (2012).
[113] E. J. Sie, J. W. McLver, Y. H. Lee, L. Fu, J. Kong, N. Gedik, "Valley-selective optical Stark effect in monolayer WS_2", *Nat. Mater.*, ***14***, 290 (2015).

한글 초록

박막 트랜지스터를 집적한 전자 디스플레이의 개발은 뛰어난 장점으로 인해 큰 관심을 받아왔다. 지난 수십 년 동안 능동 매트릭스 액정 디스플레이 및 유기 발광 다이오드와 같은 평판 디스플레이에 대한 여러 연구가 보고되었습니다. 이러한 우수한 성과에도 불구하고, p 형 산화물/나노 반도체의 개발과 백플레인 박막 트랜지스터로 구동되는 양자점 발광 다이오드의 구동에 대한 연구는 제한적입니다. p 형 반도체의 전기적 특성은 이동도가 낮고, 오프 전류가 높으며, 소자의 불안정성이 있기 때문입니다. 이러한 의미에서 우리는 앞서 언급한 응용을 위한 p-형 산화물/나노 물질 기반 박막 트랜지스터와 콜로이드 양자점 발광 다이오드를 연구했습니다.

먼저, 우리는 유연한 전자 장치에 잠재적으로 매력적인 나노 와이어 구조로 형성된 대체 전극으로 전기적 특성을 위해 스프레이 코팅된 단일벽 탄소나노튜브를 소스 및 드레인 전극으로 사용하는 p 형 주석 산화물 (SnO) 박막 트랜지스터를 구현했습니다. 폴리머 에치 스토퍼 층에 SU-8 이 있는 SnO 박막 트랜지스터의 소자 구조는 SnO 채널 층의 열화 없이 원하는 영역에서 단일벽 탄소나노튜브의 선택적 에칭을 가능하게 합니다. 또한 단일벽 탄소나노튜브 전극으로 사용하는 SnO 박막 트랜지스터는 적절한 채널폭과 정규화된 전기적 컨택 특성 (~ 1 kΩ cm), 전계 효과 이동성 (~ 0.69 cm^2/Vs), 문턱전압이하 스윙 (~ 0.4 V/dec) 및 전류 온-오프 특성 (I_{on}/I_{off} ~ 3.5×10^3)을 성공적으로 구현하였습니다. 또한 온도에 따른 전기적 컨택 및 채널 특성은 Ni 전극에 필적하는 적절한 접촉

저항과 함께 무시할 수 있는 수준의 가전자띠 테일 스테이트의 3 x 10^{-3} eV 활성화 에너지로 SnO 채널 전송을 설명합니다.

둘째, 우리는 먼저 상보형 트랜지스터를 구현하여 p (또는 n 형) $MoTe_2$ 박막 트랜지스터에 의해 제어되는 양자점 발광 다이오드 구동을 시연합니다. 이 연구에서는 $MoTe_2$ 박막 트랜지스터의 유형 변환을 위해 Poly-L-lysine (PLL)에 의한 분자 도핑을 도입하고, 양자점 발광 다이오드 성능 향상을 위해 표면 리간드 변형을 활용합니다. 이와 관련하여 PLL 처리는 전기적 특성의 저하없이 $MoTe_2$ 박막 트랜지스터의 뛰어난 유형 변환을 달성하여, 안정적인 p (또는 n 형) 유형 장치를 확보하여 보완 회로의 가용성을 보장합니다. 또한, 옥틸 아민으로 리간드 치환된 양자점은 양자점 발광 다이오드에서 균형 잡힌 전자/정공 주입을 생성하여, 전류 효율 (η_A = 13.9 cd/A)이 개선되고 수명이 더 길어집니다 (L_0 = 3000 cd/m^2 에서 T_{50} = 66 h). 결과적으로 $MoTe_2$ 박막 트랜지스터는 적절한 스위칭 특성을 가진 디스플레이 백플레인 트랜지스터, 광 전류 생성에 대한 내성 및 작동 안정성을 포함하여 양자점 발광 다이오드를 구동하는 능력을 보여줍니다.

이 논문에서 우리는 유망한 응용을 위한 산화물/나노 물질 기반 박막 트랜지스터와 리간드 치환 기술이 적용된 후면 발광 적색 양자점 발광 다이오드에 대해 논의합니다. 백플레인 박막 트랜지스로 p 형 SnO 와 $MoTe_2$ 를 사용하고, 새로운 디스플레이 장치로 CdSe 양자점 발광 다이오드를 사용한 우리의 연구 성과는 융합 연구를 위한 구상 분야에서 잠재적으로 사용될 수 있습니다.

주요어: 양자점 발광다이오드, 주석 산화물 박막 트랜지스터, 몰리브덴 디텔루라이드, 리간드 변형, 단일벽 탄소나노튜브

학번: 2017-37091

감사의 글

2017 년 가을 박사과정으로 입학하여, 4 년 동안 짧다면 짧고 길다면 긴 기간동안 독립적인 연구자로 성장하기 위해서 노력하였습니다. 이런 저에게 박사 학위를 받도록 권유해주시고, 석사과정 동안에 많은 가르침과 대학원생으로서의 자세를 가르쳐 주신 진성훈 교수님께 감사의 말씀을 드리고 싶습니다. 또한, 저를 박사 과정 학생으로 받아 주시고, 2 년 여간 지도해주신 이창희 교수님께 감사의 말씀드립니다. 방황하고 힘든 시기에 지도교수가 되어 주신 곽정훈 교수님께 감사의 인사를 드리고 싶습니다. 박사과정 동안에 교수님께서 주신 가르침을 졸업 이후에도 마음에 새기면서 하루하루 더 나아가는 연구자가 되도록 노력하겠습니다. 또한, 졸업 심사위원을 맡아 주신 홍용택 교수님과 이재상 교수님께 감사의 말씀을 드립니다. 그리고 외부심사위원으로 석사과정부터 저에게 많은 가르침을 주신 노정균 교수님과 친구이면서 연구실 선배이고, 항상 배울 점이 많은 이현호 교수님께도 감사의 인사를 드립니다.

박사과정 동안에 많은 것을 배우고, 느끼면서 같이 지내온 연구실 선후배들께 감사의 말씀드리고 싶습니다. 입학하고서 저에게 QLED 를 가르쳐 주신 희영이형, 항상 의지가 된 지호형, 동현이, 광모에게도 감사의 인사를 드리고자 합니다. 힘든 시기에도 함께 웃고 슬퍼했던 졸업하신 희범이형, 승현이, 재윤이형 감사합니다. 제 잔소리로 힘들어도 잘 따라주었던 한솔, 지현, 민형, 연준, 아영이에게도 감사하다는 말을 전하고 싶습니다. 그리고 큰형님 광근이형, 작은형님 세영이형, 태웅이형, 이수 모두들 힘들어하던 저를 이해해주시고 배려해 주셔서 감사합니다. 같이 연구하면서 힘들었을 선홍이형, 수현이, 승기, 승엽이 그리고 세미나 마다 저의 많은 질문에도 친절하게 답변해주신 영준이형, 주형이에게도 감사하다고 전하고 싶습니다. 힘들었던 시기에 연구실에서 부대끼면서 제 일도 본인 일처럼 고민해주고 얘기할 수 있는 동생들이지만 때로는 친구처럼 혹은 가족처럼 대해준 저에게는 소중한 경환, 재열, 태수,

예슬이가 있어서 4 년이라는 시간이 뜻 깊었습니다. 4 년동안 연구실에서 있었던 많은 일들이 돌이켜보면 정말 감사한 게 많아서 너무 뿌듯하고 행복합니다.

마지막으로 제가 선택하는 모든 결정에 항상 믿어 주신 엄마, 동생 근준이, 상훈이, 위광이, 건형이 앞으로 그 큰 사랑을 보답하면서 살 수 있도록 노력하겠습니다. 그리고 저에게 항상 슬플 때나 기쁠 때나 옆에서 묵묵히 응원해주고, 배려해주고, 힘을 북돋게 해준 소연이에게도 감사하다고 전하고 싶습니다. 졸업을 할 수 있게 도움주신 모든 분들께 감사의 말씀을 드리며, 더욱 더 절실하게 연구할 수 있는 사람이 되도록 노력하겠습니다.

2021 년 8 월

백 근 우